Application of Exponential-Based Methods in Integrating the Constitutive Equations with Multicomponent Nonlinear Kinematic Hardening

M. Rezaiee-Pajand[1]; Cyrus Nasirai[2]; and Mehrzad Sharifian[3]

Abstract: The von-Mises plasticity model, in the small strain regime, along with a class of multicomponent nonlinear kinematic hardening rules is considered. The material is assumed to be stabilized after several load cycles and therefore, isotropic hardening will not be accounted for. Application of exponential-based methods in integrating plasticity equations is provided, which is based on defining an augmented stress vector and using exponential maps to solve a system of quasi-linear differential equations. The solutions obtained by this new technique give very accurate updated stress values that are consistent with the yield surface. The classical forward Euler method is reformulated in details and applied to the multicomponent form of the nonlinear kinematic hardening in order to provide a comparison for the suggested technique. Moreover, a consistent tangent operator for the exponential-based integration strategy and also for the classical forward Euler algorithm is presented. In order to show the robustness and performance of the proposed formulation, an extensive numerical investigation is carried out.

DOI: 10.1061/(ASCE)EM.1943-7889.0000192

CE Database subject headings: Kinematics; Plasticity; Constitutive models; Load factors; Algorithms.

Author keywords: Exponential-based integration method; Nonlinear kinematic hardening; Cyclic plasticity; von-Mises plasticity model.

Introduction

Many structures are exposed to cyclic loads, for example, from earthquakes excitations or ocean waves. Design codes allow the use of elastic-plastic analysis to predict load effects, provided that the designer can demonstrate failure does not occur through nonlinear instabilities, excessive deformations or low cycle fatigue. Accurate prediction of structural cyclic response requires precise constitutive models to describe the complex material behavior under cyclic loads (Hopperstad and Remseth 1995).

Many efforts have been made in the last few decades to develop new models for accurate simulation of material nonlinearity. As a result, various hardening rules have been presented in the literature. Prager (1956) proposed the simplest kinematic hardening rule which was a linear relation between the incremental plastic strain and the evolution of the backstress. Prager's linear hardening rule was capable of representing the Bauschinger effect in cyclic loading. However, it failed to simulate ratcheting. In order to overcome this deficiency, two basic modifications were made to Prager's linear hardening rule. First, the idea of a multi-surface model was suggested by Besseling (1958) and Mroz (1967). In these models, multiple interacting yield surfaces were adapted and their translation was governed by a linear rule. These hardening rules presented a better response of materials, but alike other multilinear models, fail to predict ratcheting. The other modification made to Prager's rule was adding a recovery term to the linear term of the hardening law. This made the prediction of plastic strain accumulation, i.e., ratcheting, possible. The first hardening rule proposed in this category was the nonlinear hardening rule of Armstrong and Frederick (1966). Many hardening rules have been proposed ever since, using the idea of a strain hardening term and a recovery term. One of the major developments in this area was the work of Chaboche et al. (1979). Their idea was to decompose the backstress into several components and regulating each of these components to individually evolve according to an Armstrong-Frederick (AF) hardening rule. The idea of decomposing the backstress has become a main interest since. Chaboche (1991), Ohno and Wang (1993), Abdel-Karim and Ohno (2000), Kang (2004), Abdel-Karim (2009), and Rezaiee-Pajand and Sinaie (2009) later used a modified version of the original AF equation in their decomposed models.

Nonlinear finite-element analysis is an essential component of computer-aided design. In this kind of analysis, finding the answer is usually based on iterative solution of the equilibrium equations, which leads to incremental strain histories. Afterward, with the use of the material's constitutive equations, which characterize the stress as a function of the deformation history, the updated stresses are obtained. Finally, equilibrium is checked for the updated stress distribution and, if not satisfied, the iteration process is continued. One of the important steps in this process is the stress updating algorithm, which requires a large amount of calculations, even for simple constitutive models. A three-dimensional model of a solid structure may have several thousand

[1]Professor of Civil Engineering, Ferdowsi Univ. of Mashhad, Mashhad, Iran (corresponding author).

[2]Assistant Professor of Structural Engineering, Islamic Azad Univ. Mashhad Branch, Mashhad, Iran.

[3]Ph.D. Student of Structural Engineering, Ferdowsi Univ. of Mashhad, Mashhad, Iran.

Note. This manuscript was submitted on January 16, 2010; approved on May 24, 2010; published online on November 15, 2010. Discussion period open until May 1, 2011; separate discussions must be submitted for individual papers. This paper is part of the ***Journal of Engineering Mechanics***, Vol. 136, No. 12, December 1, 2010. ©ASCE, ISSN 0733-9399/2010/12-1502–1518/$25.00.

stress points at which stress updating calculations are required during each load step and in its corrective iterations. This stress updating is normally performed by numerical integration of the elastic-plastic constitutive equations.

Since cyclic inelastic analysis often leads to extensive computations, it is equally important to develop accurate, robust and efficient computational algorithms. In the past several years, new integration techniques based on the internal symmetries of simple constitutive models have been developed. The internal symmetry group of the constitutive model ensures that the plastic consistency condition will be exactly satisfied at the end of each time step if the numerical process can take it into account (Hong and Liu 1999, 2000, 2001; Liu 2003, 2004). Auricchio and Beirão da Veiga (2003) converted the original nonlinear differential problem of von-Mises plasticity with linear hardening into a dynamical system $\dot{\mathbf{X}} = \mathbb{A}\mathbf{X}$ for an augmented stress vector $\mathbf{X}$. Then, they developed a new numerical scheme by employing an exponential map, $\exp(\mathbb{A}_n \Delta t)$, as an approximation to the mentioned system. Further improvements were made to this scheme and consistent methods with a second-order accuracy were developed (Artioli et al. 2006; Rezaiee-Pajand and Nasirai 2007). By considering von-Mises plasticity with a combination of the linear isotropic and Armstrong-Frederick nonlinear kinematic hardening, Artioli et al. (2007) presented an integration algorithm based on exponential maps.

The main objective of this work is the development of an exponential-based algorithm for integrating the cyclic plasticity models. In this investigation, the cyclic plasticity model includes the von-Mises yield criterion and multicomponent nonlinear kinematic hardening. Isotropic hardening is not considered in this study, and it is assumed that the material is stabilized after several load cycles. The consistent tangent operator is derived for the suggested integration method, ensuring a quadratic rate of the asymptotic convergence, when used with the Newton-Raphson solution procedure. Moreover, the forward Euler method and its consistent tangent operator are presented to compare the results with the new exponential maps technique.

To simplify the suggested formulations, all second-order tensors are considered as nine components column vectors by ordering the tensor components in a vector format. Due to the symmetry of the second-order tensors, the number of independent components will reduce to six. It is worth emphasizing that the definition of the trace operator and the Euclidean norm must be modified.

Constitutive Models

Kinematic hardening, i.e., the translation of the yield surface in stress space, is the main primary reason for ratcheting. To complete this view, ratcheting is due to unclosed hysteresis loops. Thus, in order to develop and verify a model for ratcheting, it is essential to study the ratcheting responses of stabilized materials. This means that the parameters affecting the isotropic hardening, i.e., the change of the yield surface size, should not be included during the model development for ratcheting. Furthermore, all the kinematic hardening parameters should be determined using the experiments performed on the stabilized material. In this formulation, an associated von-Mises plasticity model with nonlinear kinematic hardening in the small strain domain is adopted. The total strain and stress, $\boldsymbol{\varepsilon}$ and $\boldsymbol{\sigma}$, are decomposed into deviatoric and volumetric components as follows:

$$\boldsymbol{\sigma} = \mathbf{s} + p\mathbf{i} \quad \text{with} \quad p = \frac{1}{3}\mathrm{tr}(\boldsymbol{\sigma}) \tag{1}$$

$$\boldsymbol{\varepsilon} = \mathbf{e} + \frac{1}{3}\varepsilon_v \mathbf{i} \quad \text{with} \quad \varepsilon_v = \mathrm{tr}(\boldsymbol{\varepsilon}) \tag{2}$$

In these relationships, tr() indicates the trace operator and $\mathbf{i}$ = vector corresponding to the second-order identity tensor. $\mathbf{s}, p, \mathbf{e}$ and ε_v are the deviatoric stress, the volumetric stress, the deviatoric strain, and the volumetric strain, respectively. The volumetric component is treated elastically by the following equation:

$$p = K\varepsilon_v \tag{3}$$

where K = material bulk modulus. The deviatoric strain is decomposed into elastic and plastic parts as follows:

$$\mathbf{e} = \mathbf{e}^e + \mathbf{e}^p \tag{4}$$

The elastic deviatoric part, $\mathbf{e}^e$, is related to the deviatoric stress by the elastic shear modulus, G, as given in the following equation:

$$\mathbf{s} = 2G\mathbf{e}^e = 2G(\mathbf{e} - \mathbf{e}^p) \tag{5}$$

For the shifted or effective stress, $\boldsymbol{\Sigma}$, the following relation is defined:

$$\boldsymbol{\Sigma} = \mathbf{s} - \boldsymbol{\alpha} \tag{6}$$

Here, $\boldsymbol{\alpha}$ = deviatoric part of the backstress and locates the center of the yield surface in the deviatoric plane. The von-Mises yield surface is as follows:

$$F = \|\boldsymbol{\Sigma}\| - R = 0 \tag{7}$$

where R = constant radius of the yield surface for a stabilized material. Rate of the deviatoric plastic strain is defined by the following equation:

$$\dot{\mathbf{e}}^p = \dot{\gamma}\mathbf{n} \tag{8}$$

The term $\dot{\gamma}$ is a proportionality factor which defines the magnitude of the deviatoric plastic strain and $\mathbf{n}$ is a vector which defines the direction of the deviatoric plastic strain, which, for an associated flow rule is normal to the yield surface at the contact point. This can be expressed in the following form:

$$\mathbf{n} = \frac{\partial F}{\partial \boldsymbol{\Sigma}} = \frac{\boldsymbol{\Sigma}}{\|\boldsymbol{\Sigma}\|} = \frac{\boldsymbol{\Sigma}}{R} \tag{9}$$

The most important feature for ratcheting simulation in cyclic plasticity constitutive models is the kinematic hardening rule, which dictates the translation of the yield surface during a plastic strain increment. In this formulation, the multicomponent form of the back stress is used as follows:

$$\dot{\boldsymbol{\alpha}} = \sum_{i=1}^{m} \dot{\boldsymbol{\alpha}}_i \tag{10}$$

where m = number of components of the deviatoric back stress vector. The nonlinear evolutionary rule of each component, $\boldsymbol{\alpha}_i$, is defined below

$$\dot{\boldsymbol{\alpha}}_i = H_{\mathrm{kin},i}\dot{\gamma}\mathbf{n} - \dot{\gamma}A_i\boldsymbol{\alpha}_i \tag{11}$$

In this equation, $H_{\mathrm{kin},i}$ = material parameters and responsible for strain hardening and A_i = scalar functions, which express the dynamic recovery of each component of deviatoric back stress. In this study, five different relations for the A_i function relevant to five well-known nonlinear kinematic hardening models are used.

These functions are given in the following lines:

1. Chaboche model (Chaboche 1986)

$$A_i = H_{\mathrm{nl},i} \tag{12}$$

2. Chaboche model with a threshold (Chaboche 1986)

$$\begin{cases} A_i = H_{\mathrm{nl},i} & \text{for } i \le 3 \\ A_i = H_{\mathrm{nl},i}\left\langle 1 - \dfrac{\bar{a}}{\|\boldsymbol{\alpha}_i\|} \right\rangle & \text{for } i = 4 \end{cases} \tag{13}$$

3. Ohno-Wang model-1 (Ohno and Wang 1993)

$$A_i = H_{\mathrm{nl},i}\left\langle \mathbf{n}^T \frac{\boldsymbol{\alpha}_i}{\|\boldsymbol{\alpha}_i\|} \right\rangle H\left\{ \boldsymbol{\alpha}_i^T \boldsymbol{\alpha}_i - \frac{3}{2}\left(\frac{H_{\mathrm{kin},i}}{H_{\mathrm{nl},i}}\right)^2 \right\} \tag{14}$$

4. Ohno-Wang model-2 (Ohno and Wang 1993)

$$A_i = H_{\mathrm{nl},i}\left\langle \mathbf{n}^{\mathrm{T}} \frac{\boldsymbol{\alpha}_i}{\|\boldsymbol{\alpha}_i\|} \right\rangle \left[\left(\frac{H_{\mathrm{nl},i}}{H_{\mathrm{kin},i}}\right) \|\boldsymbol{\alpha}_i\| \right]^{q_i} \tag{15}$$

5. AbdelKarim-Ohno model (Abdel-Karim and Ohno 2000)

$$A_i = H_{\mathrm{nl},i}\mu_i + H_{\mathrm{nl},i}\left\langle \mathbf{n}^T \frac{\boldsymbol{\alpha}_i}{\|\boldsymbol{\alpha}_i\|} - \mu_i \right\rangle H\left\{ \boldsymbol{\alpha}_i^T \boldsymbol{\alpha}_i - \frac{3}{2}\left(\frac{H_{\mathrm{kin},i}}{H_{\mathrm{nl},i}}\right)^2 \right\} \tag{16}$$

In the given equations, $\bar{a}$, q_i, $H_{\mathrm{nl},i}$, and μ_i=material parameters; H=Heaviside step function; and $\langle\ \rangle$=MacCauley bracket, i.e., $\langle x \rangle = (x+|x|)/2$. The Kuhn-Tucker loading-unloading conditions are as follows:

$$\dot{\gamma} \ge 0, \quad F \le 0, \quad \dot{\gamma}F = 0 \tag{17}$$

It should be added that plastic flow occurs if $\dot{\gamma} > 0$ and elastically when $\dot{\gamma}=0$.

Forward Euler Method

In this section, an explicit numerical scheme, called the forward Euler method, which integrates the constitutive model, will be discussed. In this method, the consistency condition must be enforced at the end of each time step. This will be done by projecting the nonconsistent final solution onto the updated yield surface.

Basic Requirements

Attaining the derivative of Eq. (6) with respect to time and using Eqs. (5), (8), and (11), the following equation is achieved:

$$\dot{\boldsymbol{\Sigma}} = 2G\dot{\mathbf{e}} - 2G\dot{\gamma}\mathbf{n} - \left(\sum_{i=1}^{m} H_{\mathrm{kin},i}\right)\dot{\gamma}\mathbf{n} - \left(\sum_{i=1}^{m} A_i \boldsymbol{\alpha}_i\right)\dot{\gamma} \tag{18}$$

Multiplying this equation by $\mathbf{n}$, and using the consistency condition, the proportionality factor $\dot{\gamma}$ can be evaluated as below

$$\dot{\gamma} = \frac{2G(\mathbf{n}^T\dot{\mathbf{e}})}{2\bar{G} - \mathbf{n}^T \sum_{i=1}^{m} A_i \boldsymbol{\alpha}_i} \tag{19}$$

where $\bar{G}$ has the following form:

$$2\bar{G} = 2G + \sum_{i=1}^{m} H_{\mathrm{kin},i} \tag{20}$$

At this stage, Eqs. (19) and (8) can be used to calculate $\dot{\gamma}$ and the deviatoric plastic strain, respectively. In the next section, an explicit integration strategy is developed.

Integration Scheme

At first, it will be assumed that the step is elastic and a trial solution for the end of the time step, i.e., t_{n+1}, is considered as follows:

$$\mathbf{e}_{n+1}^{p,\mathrm{TR}} = \mathbf{e}_n^p$$

$$\mathbf{s}_{n+1}^{\mathrm{TR}} = \mathbf{s}_n + 2G\Delta\mathbf{e}$$

$$\boldsymbol{\alpha}_{n+1}^{\mathrm{TR}} = \boldsymbol{\alpha}_n$$

$$\boldsymbol{\Sigma}_{n+1}^{\mathrm{TR}} = \mathbf{s}_{n+1}^{\mathrm{TR}} - \boldsymbol{\alpha}_{n+1}^{\mathrm{TR}} \tag{21}$$

The following relation will also be valid:

$$\Delta\mathbf{e} = \mathbf{e}_{n+1} - \mathbf{e}_n \tag{22}$$

If the trial solution is admissible, i.e., $\|\boldsymbol{\Sigma}_{n+1}^{\mathrm{TR}}\| \le R$, then the step is elastic and the final solution at the end of the load step is taken as the trial one. Otherwise, plastic correction will be needed. To do this, a scalar parameter must be calculated to divide the whole step into an elastic and a plastic phase. This scalar can be calculated by using the following relations:

$$\|2G\alpha\Delta\mathbf{e} + \mathbf{s}_n - \boldsymbol{\alpha}_n\|^2 = R^2$$

$$D\alpha^2 + 2C\alpha + M = 0$$

$$D = \|2G\Delta\mathbf{e}\|^2, \quad C = 2G\Delta\mathbf{e}^T(\mathbf{s}_n - \boldsymbol{\alpha}_n), \quad M = \|\mathbf{s}_n - \boldsymbol{\alpha}_n\|^2 - R^2$$

$$\alpha = \frac{\sqrt{C^2 - DM} - C}{D} \tag{23}$$

Afterward, the deviatoric stress and the effective stress at the contact stress point can be written as

$$\mathbf{s}^c = \mathbf{s}_n + 2G\alpha\Delta\mathbf{e}$$

$$\boldsymbol{\Sigma}^c = \mathbf{s}^c - \boldsymbol{\alpha}_n \tag{24}$$

Introducing $\lambda = \Delta\gamma = \dot{\gamma}(1-\alpha)\Delta t$, the increment of the deviatoric plastic strain can be expressed as follows:

$$\Delta\mathbf{e}^p = \lambda\mathbf{n}^c \tag{25}$$

where $\mathbf{n}^c$=normal vector to the yield surface at the contact stress point. In a fully explicit manner, by choosing the contact values for $\mathbf{n}$ and A_i in Eq. (19), the following relationship can be written:

$$\lambda = \frac{2G(\mathbf{n}^c)^T(1-\alpha)\Delta\mathbf{e}}{2\bar{G} - (\mathbf{n}^c)^T \sum_{i=1}^{m} A_i^c \boldsymbol{\alpha}_{n,i}} \tag{26}$$

Eqs. (25) and (26) will give the increment of the deviatoric plastic strain in the present load step. By using the following relations, the updated deviatoric stress and the center of the yield surface will be achieved:

$$\mathbf{s}'_{n+1} = \mathbf{s}_n + 2G(\Delta\mathbf{e} - \Delta\mathbf{e}^p)$$

$$\boldsymbol{\alpha}_{n+1,i} = \boldsymbol{\alpha}_{n,i} + H_{\text{kin},i}\Delta\mathbf{e}^p - \lambda A_i^c \boldsymbol{\alpha}_{n,i}$$

$$\boldsymbol{\alpha}_{n+1} = \sum_{i=1}^{m} \boldsymbol{\alpha}_{n+1,i} \tag{27}$$

Since the consistency condition is not automatically satisfied in this procedure, the final stress point will not be located on the yield surface. Therefore, the following correction will be made to the solution to guarantee the satisfaction of the consistency condition:

$$a_f = \sqrt{(\mathbf{n}_{n+1}^T \boldsymbol{\Sigma}'_{n+1})^2 - \|\boldsymbol{\Sigma}'_{n+1}\|^2 + R^2} - \mathbf{n}_{n+1}^T \boldsymbol{\Sigma}'_{n+1}$$

$$\boldsymbol{\Sigma}_{n+1} = \boldsymbol{\Sigma}'_{n+1} + a_f \mathbf{n}_{n+1}$$

$$\mathbf{s}_{n+1} = \mathbf{s}'_{n+1} + a_f \mathbf{n}_{n+1} \tag{28}$$

In these equations, $\mathbf{n}_{n+1}$=normal vector to the yield surface at the end of load step and a_f=parameter that enforces the consistency condition by scaling the stress vector.

Discrete Consistent Tangent Operator

An elastic-plastic tangent operator is needed to develop the structure stiffness matrix in a finite-element analysis. To achieve the quadratic rate of asymptotic convergence for Newton's technique, the tangent operator must be consistent with the numerical method employed to integrate the plasticity rate equations. Consistency implies that the updated stress predicted by the tangent operator must match the updated stress predicted by the integration procedure to the first order. By linearization of the discrete time procedure, the elastic-plastic tangent operator will be developed. This means that $(\partial\boldsymbol{\sigma}/\partial\boldsymbol{\varepsilon})_{n+1}$ is needed. Taking the derivative of Eq. (1) with respect to $\boldsymbol{\varepsilon}_{n+1}$ and considering Eqs. (3) and (6), the following relation will be achieved:

$$\frac{\partial\boldsymbol{\sigma}_{n+1}}{\partial\boldsymbol{\varepsilon}_{n+1}} = \left(\frac{\partial\boldsymbol{\Sigma}_{n+1}}{\partial\mathbf{e}_{n+1}} + \frac{\partial\boldsymbol{\alpha}_{n+1}}{\partial\mathbf{e}_{n+1}}\right)\mathbb{I}_{\text{dev}} + K(\mathbf{ii}^T) \tag{29}$$

where

$$\mathbb{I}_{\text{dev}} = \mathbb{I} - \frac{1}{3}(\mathbf{ii}^T) \tag{30}$$

At this stage, the terms $\partial\boldsymbol{\Sigma}_{n+1}/\partial\mathbf{e}_{n+1}$ and $\partial\boldsymbol{\alpha}_{n+1}/\partial\mathbf{e}_{n+1}$ in Eq. (29) must be calculated as follows:

$$\frac{\partial\boldsymbol{\Sigma}_{n+1}}{\partial\mathbf{e}_{n+1}} = \frac{\partial\boldsymbol{\Sigma}'_{n+1}}{\partial\mathbf{e}_{n+1}} + \frac{\partial a_f}{\partial\mathbf{e}_{n+1}}(\mathbf{n}_{n+1})^T + a_f\frac{\partial\mathbf{n}_{n+1}}{\partial\mathbf{e}_{n+1}} \tag{31}$$

$$\frac{\partial\boldsymbol{\alpha}_{n+1}}{\partial\mathbf{e}_{n+1}} = \sum_{i=1}^{m}\frac{\partial\boldsymbol{\alpha}_{n+1,i}}{\partial\mathbf{e}_{n+1}} \tag{32}$$

$$\frac{\partial\boldsymbol{\alpha}_{n+1,i}}{\partial\mathbf{e}_{n+1}} = H_{\text{kin},i}\frac{\partial\Delta\mathbf{e}^p}{\partial\mathbf{e}_{n+1}} - \frac{\partial\lambda}{\partial\mathbf{e}_{n+1}}(A_i^c\boldsymbol{\alpha}_{n,i})^T - \lambda\boldsymbol{\alpha}_{n,i}\left(\frac{\partial A_i^c}{\partial\mathbf{e}_{n+1}}\right)^T \tag{33}$$

The derivative of A_i^c is presented in Appendix I. Furthermore, the derivatives of the other vectors appearing in the above equations are given in Appendix II.

Exponential-Based Method

Application of exponential-based technique for integrating model equations of cyclic plasticity models will be presented in this section. First, by defining an augmented stress vector, the nonlinear differential equations of the constitutive model will be converted to a set of quasi-linear differential equations. Then, a numerical scheme based on the exponential maps is used to solve the augmented differential equation system. At the end of this section, a tangent operator consistent with the new integration algorithm is calculated.

Augmented Differential Equation System

In this section, it is intended to convert the original associated von-Mises plasticity model with nonlinear kinematic hardening, i.e., Eq. (7), into the following nonlinear differential system:

$$\dot{\mathbf{X}} = \mathbb{B}\mathbf{X} \tag{34}$$

where $\mathbf{X}$=augmented generalized stress vector with $n+1$ dimensions and has the following form:

$$\mathbf{X} = \begin{Bmatrix} X^0\bar{\boldsymbol{\Sigma}} \\ X^0 \end{Bmatrix} = \begin{Bmatrix} \mathbf{X}^s \\ X^0 \end{Bmatrix} \tag{35}$$

The parameter $\bar{\boldsymbol{\Sigma}}$ is a nondimensional effective stress vector with the following definition:

$$\bar{\boldsymbol{\Sigma}} = \frac{\boldsymbol{\Sigma}}{R} \tag{36}$$

Using Eqs. (6) and (5) leads to the following equation:

$$\boldsymbol{\Sigma} = 2G\mathbf{e} - 2G\mathbf{e}^p - \boldsymbol{\alpha} \tag{37}$$

Taking the derivative in time from the last equation and using Eqs. (10) and (11) gives the following result:

$$\dot{\boldsymbol{\Sigma}} = 2G\dot{\mathbf{e}} + \dot{\gamma}\sum_{i=1}^{m}A_i\boldsymbol{\alpha}_i - \left(\sum_{i=1}^{m}H_{\text{kin},i} + 2G\right)\dot{\mathbf{e}}^p \tag{38}$$

By inserting Eq. (8) into Eq. (38) and using Eq. (9), the following differential equation can be obtained:

$$\dot{\boldsymbol{\Sigma}} + 2\bar{G}\frac{\boldsymbol{\Sigma}}{R}\dot{\gamma} = 2G\dot{\boldsymbol{\Phi}} \tag{39}$$

where $\bar{G}$ has been given in Eq. (20) and $\dot{\boldsymbol{\Phi}}$ is defined by the following relation:

$$\dot{\boldsymbol{\Phi}} = \dot{\mathbf{e}} + \frac{\dot{\gamma}}{2G}\sum_{i=1}^{m}A_i\boldsymbol{\alpha}_i \tag{40}$$

Eq. (39) is valid for both of the elastic ($\dot{\gamma}=0$) and plastic phase. Now, using the nondimensional effective stress $\bar{\boldsymbol{\Sigma}}$, which is defined in Eq. (36), the following equation can be achieved:

$$\dot{\bar{\boldsymbol{\Sigma}}} + \frac{2\bar{G}}{R}\dot{\gamma}\bar{\boldsymbol{\Sigma}} = \frac{2G}{R}\dot{\boldsymbol{\Phi}} \tag{41}$$

At this stage, the following integrating factor, X^0, is introduced:

$$X^0\dot{\bar{\boldsymbol{\Sigma}}}+X^0\frac{2\bar{G}}{R}\dot{\gamma}\bar{\boldsymbol{\Sigma}}=\frac{d}{dt}(X^0\bar{\boldsymbol{\Sigma}}) \tag{42}$$

After taking the derivative of the last equation and comparing both of its sides, the following result is obtained:

$$\dot{X}^0=\frac{2\bar{G}}{R}\dot{\gamma}X^0 \tag{43}$$

Solving this ordinary differential equation, with the initial conditions $X^0=1$ and $\gamma=0$, leads to the following solution:

$$X^0(\gamma)=\exp\left(\frac{2\bar{G}}{R}\gamma\right) \tag{44}$$

Multiplying Eq. (41) by X^0 and comparing the result with Eq. (42), the following result is obtainable:

$$\frac{d}{dt}(X^0\bar{\boldsymbol{\Sigma}})=X^0\frac{2G}{R}\dot{\boldsymbol{\Phi}} \tag{45}$$

Now, by introducing the vector $\mathbf{X}^s=X^0\bar{\boldsymbol{\Sigma}}$, the last equation will be converted to the following form:

$$\dot{\mathbf{X}}^s=\frac{2G}{R}X^0\dot{\boldsymbol{\Phi}} \tag{46}$$

Eq. (43) indicates that during the elastic phase ($\dot{\gamma}=0$), X^0 will be constant. On the other hand, in the plastic phase, X^0 will be a variable. By taking the scalar product of Eq. (45) with the vector $\bar{\boldsymbol{\Sigma}}$, the following relationship can be proven:

$$\frac{X^0}{2}\frac{d}{dt}\|\bar{\boldsymbol{\Sigma}}\|^2+\dot{X}^0\|\bar{\boldsymbol{\Sigma}}\|^2=X^0\frac{2G}{R}\dot{\boldsymbol{\Phi}}^T\bar{\boldsymbol{\Sigma}} \tag{47}$$

Since in the plastic phase, $\|\bar{\boldsymbol{\Sigma}}\|=1$, the following equation can be derived:

$$\dot{X}^0=\frac{2G}{R}\dot{\boldsymbol{\Phi}}^TX^0\bar{\boldsymbol{\Sigma}} \tag{48}$$

Eqs. (35), (46), and (48) can be written in the compact form of $\dot{\mathbf{X}}=\mathbb{B}\mathbf{X}$, in the same way as it was presented in Eq. (34). It should be added that $\mathbb{B}$ is a control matrix as defined below

$$\mathbb{B}=\frac{2G}{R}\begin{bmatrix}\mathbb{O} & \dot{\mathbf{e}}\\ \mathbf{0}^T & 0\end{bmatrix}\quad \text{elastic phase}$$

$$\mathbb{B}=\frac{2G}{R}\begin{bmatrix}\mathbb{O} & \dot{\boldsymbol{\Phi}}\\ \dot{\boldsymbol{\Phi}}^T & 0\end{bmatrix}\quad \text{plastic phase} \tag{49}$$

In these equations, $\mathbb{O}$ and $\mathbf{0}$ are a null matrix and a null vector, respectively. It is worth emphasizing that the parameter $\dot{\gamma}$, which existed in the definition of vector $\dot{\boldsymbol{\Phi}}$ through Eq. (40), can be specified with Eq. (19).

Stress Updating Algorithm

For calculation purposes, one may approximate the specified controlled-strain path by a rectilinear strain path, such that $\dot{\mathbf{e}}$ is constant during each time step, denoted by $\dot{\mathbf{e}}_n$ at a discrete time $t=t_n$. In conventional finite-element analysis, the constitutive quantities at time t_n, such as $\mathbf{s}_n$, $\mathbf{e}_n$, γ_n, and $\boldsymbol{\alpha}_n$ are all known and the updated strain, $\mathbf{e}_{n+1}$, is also known at the time $t=t_{n+1}$. The suggested numerical algorithm must integrate the plasticity rate equations over the time increment to determine the updated stress and constitutive quantities. This means solving the system of differential Eq. (34) with the following initial value:

$$\mathbf{X}_0=\begin{Bmatrix}\mathbf{X}_0^s\\ 1\end{Bmatrix}=\begin{Bmatrix}\dfrac{\boldsymbol{\Sigma}_0}{R}\\ 1\end{Bmatrix} \tag{50}$$

The solution of the dynamical system (34) is available in power series' form or in a more compact *exponential maps* form, as follows:

$$\mathbf{X}_{n+1}=\exp(\Delta t\mathbb{B})\mathbf{X}_n \tag{51}$$

In the elastic phase, the control matrix $\mathbb{B}$ is constant and $\Delta t\mathbb{B}$ may be written as follows:

$$\Delta t\mathbb{B}=\Delta t\mathbb{B}^e=\frac{2G}{R}\begin{bmatrix}\mathbb{O} & \Delta\mathbf{e}\\ \mathbf{0}^T & 0\end{bmatrix} \tag{52}$$

where $\Delta\mathbf{e}=\Delta t\dot{\mathbf{e}}=\mathbf{e}_{n+1}-\mathbf{e}_n$ is the strain rate vector. On the other hand, the control matrix $\mathbb{B}$ will not be constant during the plastic phase. However, in a fully explicit manner one may assume that $\mathbb{B}$ is constant during each Δt time step. The known value of $\mathbb{B}$ at the beginning of each time step, $\mathbb{B}_n$, is the value considered throughout the time interval. This can be expressed as follows:

$$\mathbf{X}_{n+1}=\exp(\Delta t\mathbb{B}_n)\mathbf{X}_n=\mathbb{G}_n\mathbf{X}_n \tag{53}$$

In the plastic phase, $\Delta t\mathbb{B}_n$ can be expressed as follows:

$$\Delta t\mathbb{B}_n=\frac{2G}{R}\begin{bmatrix}\mathbb{O} & \Delta\boldsymbol{\Phi}\\ \Delta\boldsymbol{\Phi}^T & 0\end{bmatrix} \tag{54}$$

$$\Delta\boldsymbol{\Phi}=\Delta\mathbf{e}+\frac{\mathbf{n}_n^T\Delta\mathbf{e}}{2\bar{G}-\mathbf{n}_n^T\sum_{i=1}^{m}A_{n,i}\boldsymbol{\alpha}_i}\sum_{i=1}^{m}A_{n,i}\boldsymbol{\alpha}_{n,i} \tag{55}$$

As a result, the following relationships will be valid:

$$\mathbb{G}^e=\begin{bmatrix}\mathbb{I} & \dfrac{2G}{R}\Delta\mathbf{e}\\ \mathbf{0}^T & 1\end{bmatrix}\quad \text{elastic step} \tag{56}$$

$$\mathbb{G}^p=\begin{bmatrix}\mathbb{I}+(a-1)\Delta\hat{\boldsymbol{\Phi}}\Delta\hat{\boldsymbol{\Phi}}^T & b\Delta\hat{\boldsymbol{\Phi}}\\ b\Delta\hat{\boldsymbol{\Phi}}^T & a\end{bmatrix}\quad \text{plastic step} \tag{57}$$

$$\Delta\hat{\boldsymbol{\Phi}}=\frac{\Delta\boldsymbol{\Phi}}{\|\Delta\boldsymbol{\Phi}\|} \tag{58}$$

$$a=\cosh(g);\quad b=\sinh(g);\quad g=\frac{2G}{R}\|\Delta\boldsymbol{\Phi}\| \tag{59}$$

Updating the Center of the Yield Surface

At the end of a time step, the center of the yield surface must be updated. By integrating Eq. (11), the following relations will be achieved:

$$\boldsymbol{\alpha}_{n+1,i}-\boldsymbol{\alpha}_{n,i}=\int_{t_n}^{t_{n+1}}(H_{\mathrm{kin},i}\dot{\mathbf{e}}^p-\dot{\gamma}A_i\boldsymbol{\alpha}_i)dt \tag{60}$$

As it is clear in Eq. (12), the parameter A_i is a constant scalar in the Chaboche model. It should be reminded that for the other nonlinear kinematic hardening models which are presented in Eqs. (13)–(16), A_i will not be constant. If it is assumed that A_i is constant during each time step, i.e., $A_i = A_{i,n}$, and $\boldsymbol{\alpha}_i$ be approximated by its values at the start and end of the time step, i.e., $\boldsymbol{\alpha}_i = 1/2(\boldsymbol{\alpha}_{n,i} + \boldsymbol{\alpha}_{n+1,i})$, Eq. (60) will lead to the following form:

$$\boldsymbol{\alpha}_{n+1,i} - \boldsymbol{\alpha}_{n,i} = H_{\text{kin},i}\Delta\mathbf{e}^p - \frac{\lambda}{2}A_i(\boldsymbol{\alpha}_{n,i} + \boldsymbol{\alpha}_{n+1,i}) \quad (61)$$

In this equation, $\lambda = \gamma_{n+1} - \gamma_n$. By using Eq. (44), the following result can be found:

$$\lambda = \frac{R}{2\bar{G}}\ln\left(\frac{X^0_{n+1}}{X^0_n}\right) \quad (62)$$

Manipulating Eq. (61) will lead to the following result:

$$\boldsymbol{\alpha}_{n+1,i} = \frac{1}{2 + \lambda A_i}[2H_{\text{kin},i}\Delta\mathbf{e}^p + (2 - \lambda A_i)\boldsymbol{\alpha}_{n,i}] \quad (63)$$

Summing the components of the back stress vector in Eq. (63) leads to the following equation for the center of the yield surface:

$$\boldsymbol{\alpha}_{n+1} = \bar{H}_{\text{kin}}\Delta\mathbf{e}^p + \mathbf{a} \quad (64)$$

where the other parameters are as follows:

$$\bar{H}_{\text{kin}} = \sum_{i=1}^{m}\frac{2H_{\text{kin},i}}{2 + \lambda A_i} \quad (65)$$

$$\mathbf{a} = \sum_{i=1}^{m}\frac{2 - \lambda A_i}{2 + \lambda A_i}\boldsymbol{\alpha}_{n,i} \quad (66)$$

Using $\boldsymbol{\Sigma}_{n+1} = \mathbf{s}_{n+1} - \boldsymbol{\alpha}_{n+1}$ along with Eq. (64), the following equation for $\Delta\mathbf{e}^p$ will be achieved:

$$\Delta\mathbf{e}^p = \frac{1}{2G + \bar{H}_{\text{kin}}}(\mathbf{s}_n + 2G\Delta\mathbf{e} - \mathbf{a} - \boldsymbol{\Sigma}_{n+1}) \quad (67)$$

Finally, inserting the above relation into Eqs. (64) and (63), the back stress vector and its components at the end of the load step can be calculated.

Elastic-Plastic Steps

Like many predictor-corrector integration algorithms, each step is started by computing a trial value of the augmented stress vector, by assuming an elastic behavior, as follows:

$$\mathbf{X}^{\text{TR}}_{n+1} = \mathbb{G}^e\mathbf{X}_n \quad (68)$$

If the trial estimation is admissible, i.e., $\|\mathbf{X}^{s,\text{TR}}_{n+1}\| \le X^{0,\text{TR}}_{n+1}$, then the variables at time t_{n+1} are taken as the trial values. Note that $X^{0,\text{TR}}_{n+1}$ is equal to X^0_n, since in the elastic prediction X^0 is not changed. If the trial solution is not admissible, then the step is plastic. Therefore, this step can be divided into two parts: an elastic deformation, followed by a plastic deformation. Parameter α, which denotes the elastic and the plastic parts of such a step, can be calculated with the use of Eq. (23). Parameters C, D, and M in the augmented stress space could be presented as follows:

$$D = \left(\frac{2G}{R}X^0_n\|\Delta\mathbf{e}\|\right)^2; \quad C = \frac{2G}{R}X^0_n(\mathbf{X}^s_n)^T\Delta\mathbf{e}; \quad M = \|\mathbf{X}^s_n\|^2 - (X^0_n)^2 \quad (69)$$

The contact stress augmented stress vector which is related to the intersection of stress path with the yield surface can be computed by the following equations:

$$\mathbf{X}^c = \mathbb{G}^c\mathbf{X}_n \quad (70)$$

$$\mathbb{G}^c = \begin{bmatrix} \mathbb{I} & \frac{2G}{R}\alpha\Delta\mathbf{e} \\ \mathbf{0}^T & 1 \end{bmatrix} \quad (71)$$

Since $(1-\alpha)\Delta\mathbf{e}$ denotes a fully plastic step, the updated stress at the end of the time step can still be computed by Eq. (57) with the following modifications:

$$g = \frac{2G}{R}\|(1-\alpha)\Delta\boldsymbol{\Phi}\| \quad (72)$$

$$\Delta\boldsymbol{\Phi} = \Delta\mathbf{e} + \frac{(\mathbf{n}^c)^T\Delta\mathbf{e}}{2\bar{G} - (\mathbf{n}^c)^T\sum_{i=1}^{m}A^c_i\boldsymbol{\alpha}_{n,i}}\sum_{i=1}^{m}A^c_i\boldsymbol{\alpha}_{n,i} \quad (73)$$

where A^c_i = value of A_i at the contact stress point, i.e., $A^c_i = A_i(\boldsymbol{\alpha}_n, \mathbf{n}^c)$.

Discrete Consistent Tangent Operator

In this section, it is intended to present the tangent operator that is consistent with the new exponential-based integration scheme. Referring to Eq. (29), the terms $\partial\boldsymbol{\Sigma}_{n+1}/\partial\mathbf{e}_{n+1}$ and $\partial\boldsymbol{\alpha}_{n+1}/\partial\mathbf{e}_{n+1}$ must be calculated. Using the definition of $\mathbf{X}^s = X^0\bar{\boldsymbol{\Sigma}}$ and referring to Eq. (36), the following equality will be valid:

$$\mathbf{X}^s_{n+1} = \frac{X^0_{n+1}}{R}\boldsymbol{\Sigma}_{n+1} \quad (74)$$

Attaining the derivative of the last equation with respect to $\mathbf{e}_{n+1}$, gives the below result:

$$\frac{\partial\mathbf{X}^s_{n+1}}{\partial\mathbf{e}_{n+1}} = \frac{\boldsymbol{\Sigma}_{n+1}}{R}\left(\frac{\partial X^0_{n+1}}{\partial\mathbf{e}_{n+1}}\right)^T + \frac{X^0_{n+1}}{R}\frac{\partial\boldsymbol{\Sigma}_{n+1}}{\partial\mathbf{e}_{n+1}} \quad (75)$$

Manipulating Eq. (75), leads to the following relation:

$$\frac{\partial\boldsymbol{\Sigma}_{n+1}}{\partial\mathbf{e}_{n+1}} = \frac{R}{X^0_{n+1}}\frac{\partial\mathbf{X}^s_{n+1}}{\partial\mathbf{e}_{n+1}} - \frac{R}{(X^0_{n+1})^2}\left[\mathbf{X}^s_{n+1}\left(\frac{\partial X^0_{n+1}}{\partial\mathbf{e}_{n+1}}\right)^T\right] \quad (76)$$

At this stage, the derivatives of $\mathbf{X}^s_{n+1}$ and X^0_{n+1} are needed. Using Eq. (53) and assuming a general elastic-plastic load step, the following equations can be written:

$$\mathbf{X}_{n+1} = \mathbb{G}^p\mathbb{G}^e\mathbf{X}_n \quad (77)$$

$$\begin{aligned}\mathbf{X}^s_{n+1} = {} & \mathbf{X}^s_n + (a-1)(\Delta\hat{\boldsymbol{\Phi}}^T\mathbf{X}^s_n)\Delta\hat{\boldsymbol{\Phi}} + \alpha\frac{2G}{R}X^0_n\Delta\mathbf{e} \\ & + (a-1)\alpha\frac{2G}{R}X^0_n(\Delta\hat{\boldsymbol{\Phi}}^T\Delta\mathbf{e})\Delta\hat{\boldsymbol{\Phi}} + bX^0_n\Delta\hat{\boldsymbol{\Phi}} \end{aligned} \quad (78)$$

$$X_{n+1}^0 = b(\Delta\hat{\boldsymbol{\Phi}}^T\mathbf{X}_n^s) + b\alpha\frac{2G}{R}X_n^0(\Delta\hat{\boldsymbol{\Phi}}^T\Delta\mathbf{e}) + aX_n^0 \tag{79}$$

As it is seen, the derivatives of the mentioned terms are far more complicated. These expressions are presented in Appendix III. On the other hand, addressing Eq. (63), to completely define the derivative of $\boldsymbol{\alpha}_{n+1}$, the derivatives of its components must be driven as follows:

$$\begin{aligned}\frac{\partial\boldsymbol{\alpha}_{n+1,i}}{\partial\mathbf{e}_{n+1}} &= \frac{2H_{\mathrm{kin},i}}{2+\lambda A_i^c}\frac{\partial\Delta\mathbf{e}^p}{\partial\mathbf{e}_{n+1}} - \frac{A_i^c}{2+\lambda A_i^c}\left[\boldsymbol{\alpha}_{n,i}\left(\frac{\partial\lambda}{\partial\mathbf{e}_{n+1}}\right)^T\right]\\ &\quad - \frac{\lambda}{2+\lambda A_i^c}\left[\boldsymbol{\alpha}_{n,i}\left(\frac{\partial A_i^c}{\partial\mathbf{e}_{n+1}}\right)^T\right]\\ &\quad - A_i^c\frac{2H_{\mathrm{kin},i}\Delta\mathbf{e}^p + (2-\lambda A_i^c)\boldsymbol{\alpha}_{n,i}}{(2+\lambda A_i^c)^2}\left(\frac{\partial\lambda}{\partial\mathbf{e}_{n+1}}\right)^T\\ &\quad - \lambda\frac{2H_{\mathrm{kin},i}\Delta\mathbf{e}^p + (2-\lambda A_i^c)\boldsymbol{\alpha}_{n,i}}{(2+\lambda A_i^c)^2}\left(\frac{\partial A_i^c}{\partial\mathbf{e}_{n+1}}\right)^T\end{aligned} \tag{80}$$

The derivatives of parameter λ and vector $\Delta\mathbf{e}^p$, which appeared in the last equation, can be calculated referring to Eqs. (62) and (67), respectively. These are given below

$$\frac{\partial\lambda}{\partial\mathbf{e}_{n+1}} = \frac{R}{2\bar{G}}\frac{1}{X_{n+1}^0}\frac{\partial X_{n+1}^0}{\partial\mathbf{e}_{n+1}} \tag{81}$$

$$\begin{aligned}\frac{\partial\Delta\mathbf{e}^p}{\partial\mathbf{e}_{n+1}} &= -\frac{1}{(2G+\bar{H}_{\mathrm{kin}})^2}(\mathbf{s}_n + 2G\Delta\mathbf{e} - \mathbf{a} - \boldsymbol{\Sigma}_{n+1})\left(\frac{\partial\bar{H}_{\mathrm{kin}}}{\partial\mathbf{e}_{n+1}}\right)^T\\ &\quad + \frac{1}{2G+\bar{H}_{\mathrm{kin}}}\left(2G\mathbb{I} - \frac{\partial\mathbf{a}}{\partial\mathbf{e}_{n+1}} - \frac{\partial\boldsymbol{\Sigma}_{n+1}}{\partial\mathbf{e}_{n+1}}\right)\end{aligned} \tag{82}$$

To calculate the derivatives of parameter $\bar{H}_{\mathrm{kin}}$ and also vector $\mathbf{a}$, Eqs. (65) and (66) are used. Finally, the results are as follows:

$$\frac{\partial\bar{H}_{\mathrm{kin}}}{\partial\mathbf{e}_{n+1}} = -\sum_{i=1}^{m}\frac{2\lambda H_{\mathrm{kin},i}}{(2+\lambda A_i^c)^2}\frac{\partial A_i^c}{\partial\mathbf{e}_{n+1}} - \sum_{i=1}^{m}\frac{2A_i^cH_{\mathrm{kin},i}}{(2+\lambda A_i^c)^2}\frac{\partial\lambda}{\partial\mathbf{e}_{n+1}} \tag{83}$$

$$\begin{aligned}\frac{\partial\mathbf{a}}{\partial\mathbf{e}_{n+1}} &= -\sum_{i=1}^{m}\frac{4\lambda}{(2+\lambda A_i^c)^2}\left[\boldsymbol{\alpha}_{n,i}\left(\frac{\partial A_i^c}{\partial\mathbf{e}_{n+1}}\right)^T\right]\\ &\quad - \sum_{i=1}^{m}\frac{4A_i^c}{(2+\lambda A_i^c)^2}\left[\boldsymbol{\alpha}_{n,i}\left(\frac{\partial\lambda}{\partial\mathbf{e}_{n+1}}\right)^T\right]\end{aligned} \tag{84}$$

The derivative of A_i^c is presented in Appendix I.

Numerical Examples

An elastic-plastic constitutive relationship depends on deformation history. Therefore, an incremental analysis is needed to trace the variation of displacement, strain and stress along with the external forces. In each load step, the equilibrium of the external force and equivalent force of stress acting on nodal points must be satisfied. In fact, two processes are involved in solving nonlinear equilibrium equation. In the first one, the algorithm is used for solving nonlinear simultaneous equations. Most of these approaches are Newton like and need tangential stiffness matrix of structure for a fast convergence. To establish the structural stiffness matrix, a tangent operator, i.e., $\partial\boldsymbol{\sigma}/\partial\boldsymbol{\varepsilon}$, at each sample point of elements must be calculated. Another main action is the integration scheme. For a given stress state and deformation history, this algorithm is used to determine the stress increment, $\Delta\boldsymbol{\sigma}$, which corresponds to a strain increment, $\Delta\boldsymbol{\varepsilon}$. The integration procedure must be performed at every gauss point of elements for each load step and corrective iterations as well. The tangent operator which is used in the first algorithm must be consistent with the integration scheme of the second one.

This study is focused on the integration scheme, and all numerical presentations are pointwise. The selected problems can be classified in three categories. In the first one, i.e., stress updating examples, an input strain history is assumed and the stress output will be calculated. In this category, accuracy and rate of convergence of the presented integration strategy are explored through a piecewise strain history using different time steps. In the second category, i.e., strain updating examples, an input stress history is considered and the strain history will be computed. Here, the objective is to validate the tangent operator through a Newton like, path independent strategy. In the third category, a mixed type control example with some components of stress controlled and also the other components of strain controlled will be presented.

All the strain and stress paths are considered linear to eradicate the discretization errors. It must be mentioned that, each integration scheme operates under the restriction of a constant strain rate vector. For a finite size load step, this leads to a linear approximation of a curved path. The use of this approximation introduces discretization errors. These errors are in addition to the ones from the integration of the plasticity rate equations.

In order to show the robustness of the suggested exponential-based formulation, all the outputs are compared with the results of the classical forward Euler method. Lacking the exact solution of the investigated problems, the classical forward Euler technique with a very fine load step ($\Delta t = 1\times10^{-5}$ s) is used to produce required exact solutions. As it is intended to get reasonable results, mechanical characteristics of a kind of carbon steel (CS1026) is adopted. The material is considered to be stabilized and no isotropic hardening is available. The general parameters of stabilized CS1026 are as follows (Bari and Hassan 2000):

$$E = 181{,}330\ \text{MPa};\quad R = 106\ \text{MPa};\quad \nu = 0.302$$

To avoid lengthening, only three different ratcheting models, which are the most common ones, are chosen. The characteristics for these models and the acronyms that are used in the numerical presentations are as follows (Bari and Hassan 2000):

1. **Ch3:** Chaboche model-three decomposed rule

$$H_{\mathrm{kin},1-3} = 275{,}792/59{,}093/2{,}091\ \text{MPa}$$

$$H_{\mathrm{nl},1-3} = 16{,}330/653/7$$

2. **Ch4T:** Chaboche model-fourth rule with a threshold

$$H_{\mathrm{kin},1-4} = 275{,}792/59{,}093/2{,}091\ \text{MPa}$$

$$H_{\mathrm{nl},1-4} = 16{,}330/653/9/4{,}082$$

$$\bar{a} = 28\ \text{MPa}$$

3. **OW:** Ohno-Wang model-2 with 12 segments

$$H_{\mathrm{kin},1-12} = 146{,}813/166{,}459/11{,}583/1{,}728/50{,}658/20{,}919/15{,}973/10{,}094/3{,}939/1{,}135/450/919\ \text{MPa}$$

$$H_{\mathrm{nl},1-12} = 36{,}908/11{,}385/6{,}310/4{,}046/3{,}015/1{,}743/1{,}004/478/241/97/41/16$$

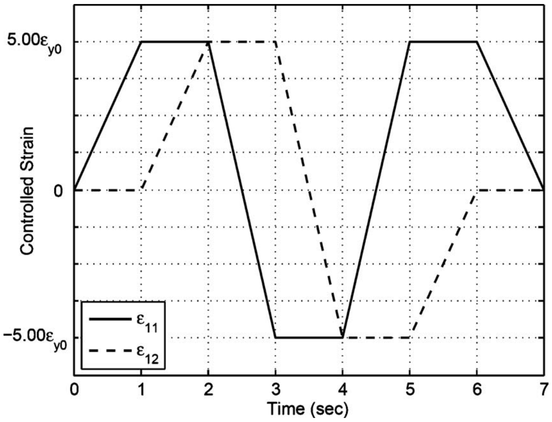

Fig. 1. Strain components history for Path 1

Stress Updating Examples

A biaxial nonproportional strain path is considered. The strain components' histories and the corresponding path are represented graphically in Figs. 1 and 2. In these figures, the parameter ε_{y0} is the first yielding strain in a uniaxial loading history, i.e., $\varepsilon_{y0} = \sqrt{3/2}(R/E)$. All the other strain components are equal to zero. The updated stress history corresponding to this strain history is calculated with the new exponential-based method and also with the forward Euler algorithm for the sake of comparison. The results are achieved using a practical load step size ($\Delta t = 0.0125$ sec). The nondimensional or relative error of the updated stress is defined by the following equation:

$$E_n^{\sigma} = \frac{\|\boldsymbol{\sigma}_n - \boldsymbol{\sigma}_n^*\|}{R} \tag{85}$$

where $\boldsymbol{\sigma}_n^*$=exact stress vector at time t_n. Figs. 3–5 show the accuracy of the exponential maps scheme in comparison with the classical forward Euler method for three different nonlinear kinematic hardening models. The diagrams show that the proposed exponential-based strategy gives a better approximation of the updated stress. It must be mentioned that the assumed load step is the largest one that allows the forward Euler method to converge. As it can be seen in Fig. 5, in the Ohno-Wang hardening model, even with this load step, the classical technique diverges. In order

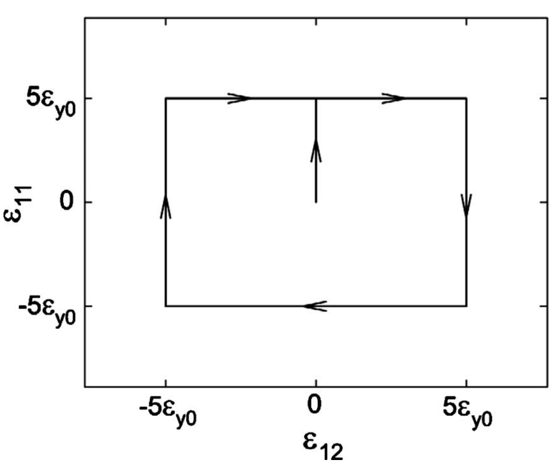

Fig. 2. Strain Path 1

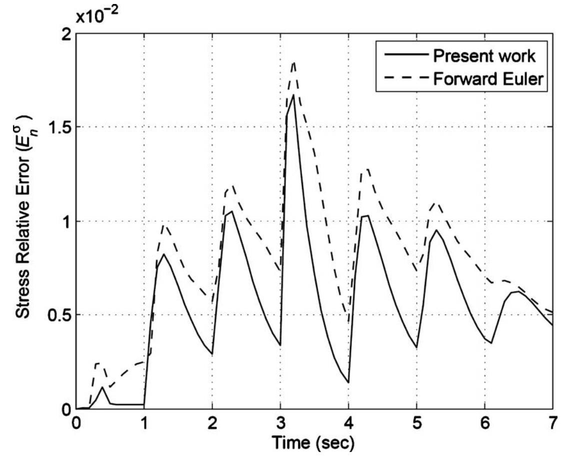

Fig. 3. Stress relative error of Path 1, Ch3, $\Delta t = 0.0125$ s

to better investigate the rate of convergence of these algorithms, the average total error is introduced as follows:

$$E_T^{\sigma} = \frac{1}{N}\sum_{n=1}^{N} \frac{\|\boldsymbol{\sigma}_n - \boldsymbol{\sigma}_n^*\|}{R} \tag{86}$$

where the parameter N=total number of the load steps. By adopting different size of the load steps, the total error is computed for

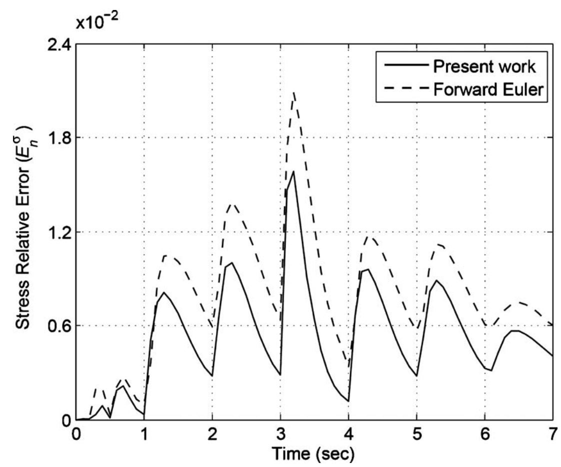

Fig. 4. Stress relative error of Path 1, Ch4T, $\Delta t = 0.0125$ s

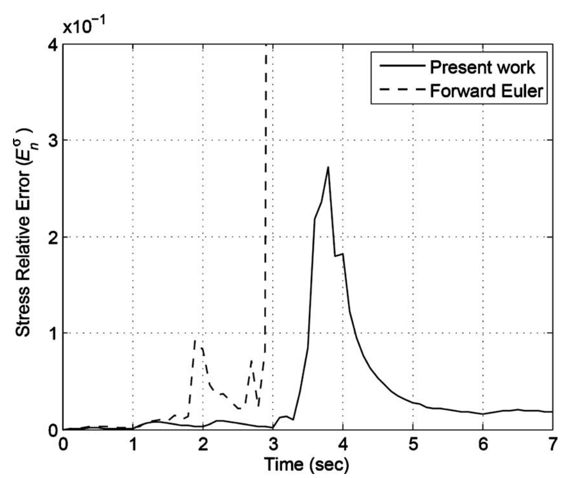

Fig. 5. Stress relative error of Path 1, OW, $\Delta t = 0.0125$ s

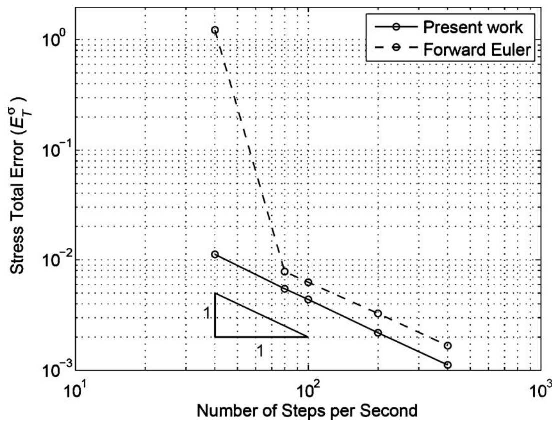

Fig. 6. Stress total error of Path 1, Ch3

both schemes assuming the Ch3 kinematic hardening model. Afterwards, the results are plotted in Fig. 6. It is easy to find, in a logarithmic space of this diagram, the relationship between the total error and the number of substeps is linear. The slope of each line represents the convergence rate of the corresponding procedure. It shows that, although both algorithms have first order accuracy, but the classical method will diverge with the large load steps.

For a better demonstration of the performance of the new formulation, another nonproportional strain history is considered. This history and its path are presented in Figs. 7 and 8, respectively. The accuracy of the suggested exponential maps scheme in comparison with the classical forward Euler method is shown in Figs. 9–11. Like the previous example, three different nonlinear kinematic hardening models are considered. It is evident that the updated stresses calculated by the new method have better accuracy.

At this stage, it is intended to test computation time for three different integration algorithms. In a pointwise problem, the computation time on a normal CPU for a single stress point is very short. To give a measurable CPU time, the strain history of Fig. 1 is repeated 50 times with a total time of 350 s. For a convincible demonstration, the formulation of backward Euler method, which is an implicit algorithm and was presented comprehensively by Kobayashi and Ohno (2002), is also tested. The total error in all three strategies is kept the same. Results are presented in Table 1. The proposed algorithm requires the shortest computation time

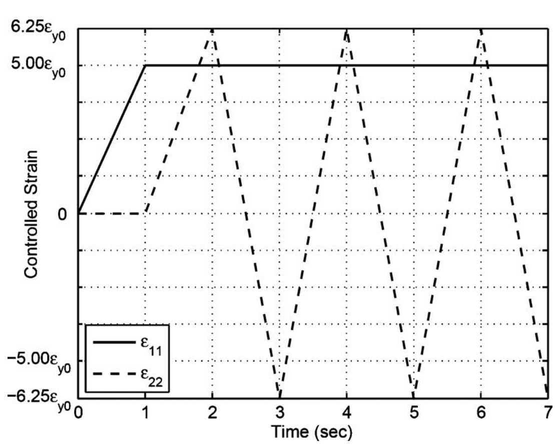

Fig. 7. Strain components history for Path 2

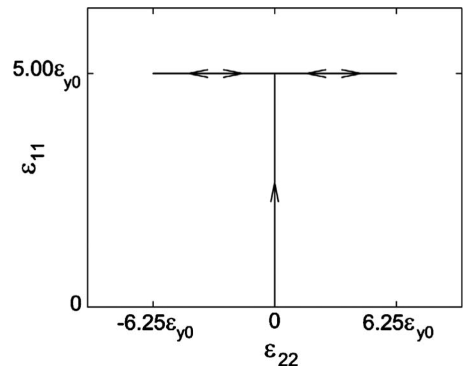

Fig. 8. Strain Path 2

and runs about 19% faster than the forward Euler method, which is known as a rapid scheme. The longer CPU time of the backward Euler method is due to its inherence iterative loops.

Strain Updating Examples

In these pointwise problems, the objective is to test the second-order convergence rate of the elastoplastic consistent tangent, through a Newton algorithm in a load-driven manner with the iterative process. A biaxial nonproportional stress history is con-

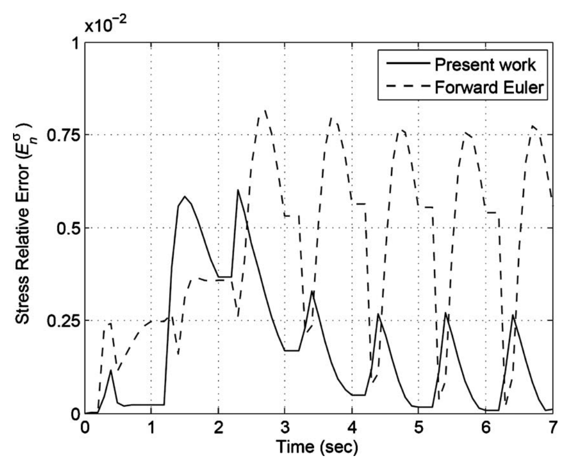

Fig. 9. Stress relative error of Path 2, Ch3, $\Delta t = 0.0125$ s

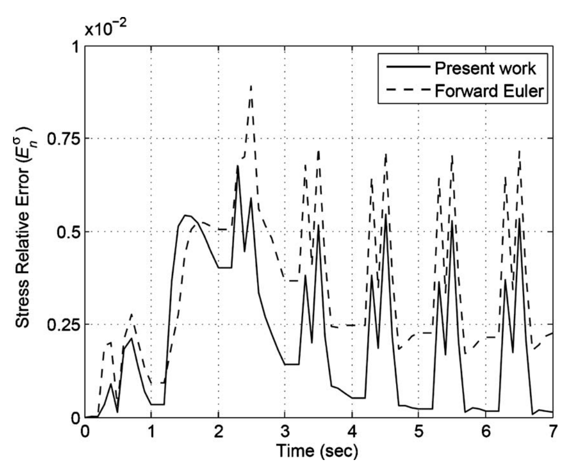

Fig. 10. Stress relative error of Path 2, Ch4T, $\Delta t = 0.0125$ s

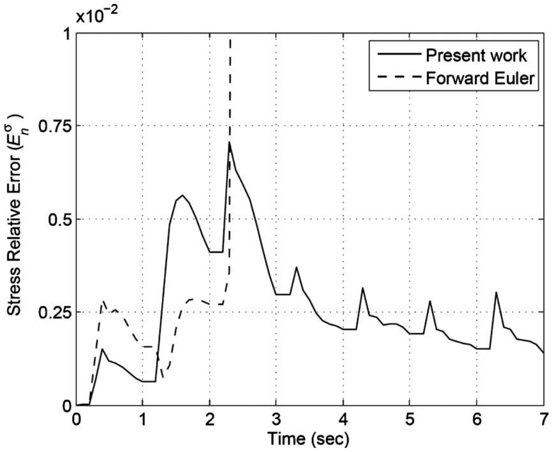

Fig. 11. Stress relative error of Path 2, OW, $\Delta t = 0.0125$ s

sidered as input, which is graphically represented in Fig. 12. In addition, the corresponding stress path is shown in Fig. 13. All other stress components are assumed to be equal to zero. The strain history corresponding to this stress history is updated. The results are obtained by the new exponential-based scheme and also with the forward Euler algorithm that is used for assessment. A practical time discritization with the size of $\Delta t = 0.0125$ s is used. The nondimensional or relative error for the updated strain can be defined by the following equation:

$$E_n^{\varepsilon} = 2G\frac{\|\boldsymbol{\varepsilon}_n - \boldsymbol{\varepsilon}_n^*\|}{R} \tag{87}$$

where $\boldsymbol{\varepsilon}_n^*$=exact strain vector at time t_n and $\boldsymbol{\varepsilon}_n$=numerical solution. Figs. 14–16 show the accuracy of the exponential maps formulation in comparison with the classical forward Euler method for three different nonlinear kinematic hardening models.

Table 1. Efficiency of the Algorithms for 50 Cycles of the Strain Path 1

Algorithm	Step per second	Total steps	CPU time (s)
Exponential maps, present study	50	17,500	3.42
Forward Euler, present study	80	28,000	4.08
Backward Euler, Kobayashi and Ohno (2002)	80	28,000	10.43

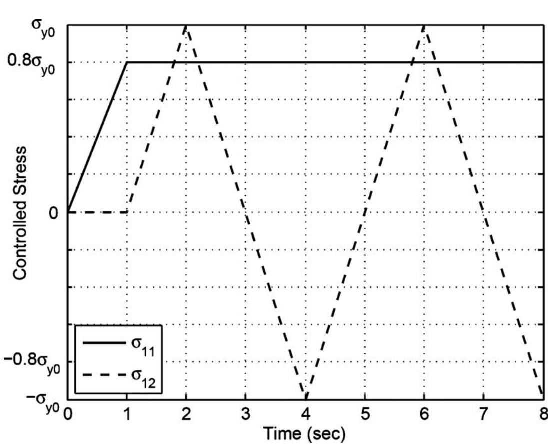

Fig. 12. Stress components history for Path 1

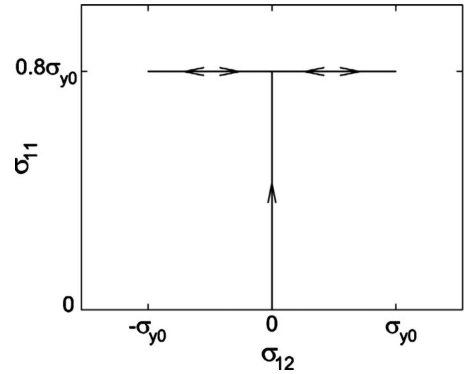

Fig. 13. Stress Path 1

As it is clearly seen from these figures, better approximation of the updated strain is computed by the exponential-based method. To examine the rate of convergence, the relative Euclidean norms of error in the Newton iterations for each time step are defined by the following relation:

$$E_n^i = \frac{\|\boldsymbol{\varepsilon}_n^i - \boldsymbol{\varepsilon}_n\|}{\|\boldsymbol{\varepsilon}_n^1 - \boldsymbol{\varepsilon}_n\|} \tag{88}$$

where $\boldsymbol{\varepsilon}_n$ and $\boldsymbol{\varepsilon}_n^i$=convergence strain and its ith estimation in time t_n, respectively. To demonstrate the second-order convergence of

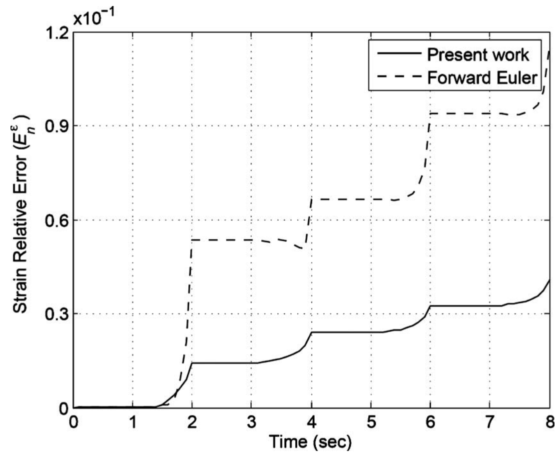

Fig. 14. Strain relative error of Path 1, Ch3, $\Delta t = 0.0125$ s

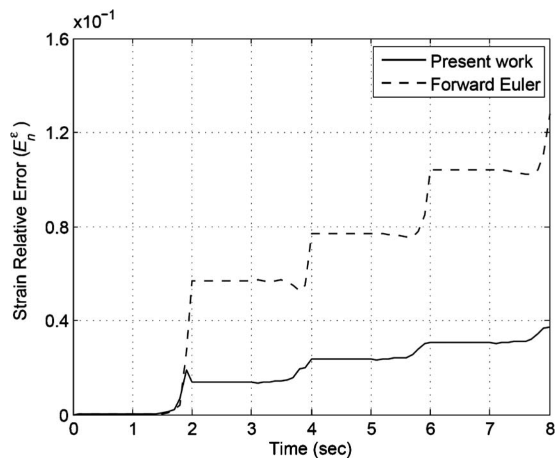

Fig. 15. Strain relative error of Path 1, Ch4T, $\Delta t = 0.0125$ s

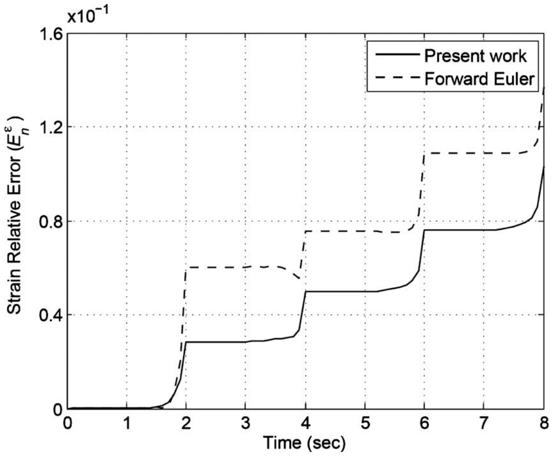

Fig. 16. Strain relative error of Path 1, OW, $\Delta t = 0.0125$ s

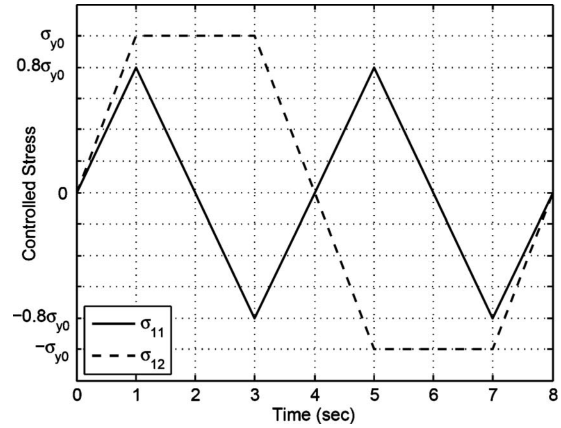

Fig. 17. Stress components history for Path 2

tangent operators, which is used in the Newton method, the relative Euclidean norms E_{n+1}^i is presented in Tables 2–4 for successive iterations in two arbitrary times $t=4$ s and $t=8$ s for stress Path 1 and assuming Ch3, Ch4T, and OW kinematic hardening models. These tables show that the developed technique has a quadratic convergence rate.

For a better demonstration of the performance of the new algorithm, another stress history is considered. This history and its path are presented in Figs. 17 and 18, respectively. The accuracy of the exponential maps scheme in comparison with the classical forward Euler method is shown in Figs. 19–21. Like the previous example, three different nonlinear kinematic hardening models are considered. It is clear that the updated strains calculated with the exponential-based method have better accuracy.

The assumed multicomponent nonlinear kinematic hardening models have the ability to predict ratcheting. In the following, an example is presented to verify the facility of the new numerical algorithm in predicting ratcheting. A broad set of the ratcheting data, which includes uniaxial to complex biaxial ratcheting responses of the stabilized carbon steels, have been developed by Hassan and Kyriakides (1994a,b). The prescribed cyclic loading history is shown in Fig. 22. This diagram involves the unsymmetrical axial stress cycles with a mean stress $\sigma_m = 45$ MPa and an amplitude stress $\sigma_a = 220$ MPa. The simulation for a single stress-controlled hysteresis loop by the Chaboche model using three decomposed rules (Ch3) is carried out. Forward Euler method and the new exponential-based scheme, with a practical load step of the size $\Delta t = 0.01$ s, are used and the results are compared with the exact solution. As it was mentioned before, the exact solution is computed by the classical forward Euler with $\Delta t = 1 \times 10^{-5}$ s. Fig. 23 shows that the responses of the new numerical strategy are very close to the exact solution, even with the

Table 2. Typical Convergence Value, the Relative Euclidean Norms for Stress Path 1, Ch3

	$t=4$ s		$t=8$ s	
Iteration	Present work	Forward Euler	Present work	Forward Euler
1	$1.0000 \times 10^{+00}$	$1.0000 \times 10^{+00}$	$1.0000 \times 10^{+00}$	$1.0000 \times 10^{+00}$
2	1.9425×10^{-02}	7.5063×10^{-03}	1.7301×10^{-02}	7.0197×10^{-03}
3	6.9269×10^{-04}	1.2485×10^{-04}	6.5925×10^{-04}	8.6491×10^{-05}
4	1.5624×10^{-06}	8.6073×10^{-08}	1.0787×10^{-06}	4.4021×10^{-08}
5	1.3229×10^{-09}	6.3856×10^{-10}	8.0845×10^{-10}	2.2237×10^{-10}

Table 3. Typical Convergence Value, the Relative Euclidean Norms for Stress Path 1, Ch4T

	$t=4$ s		$t=8$ s	
Iteration	Present work	Forward Euler	Present work	Forward Euler
1	$1.0000 \times 10^{+00}$	$1.0000 \times 10^{+00}$	$1.0000 \times 10^{+00}$	$1.0000 \times 10^{+00}$
2	1.9688×10^{-02}	7.8751×10^{-03}	1.7362×10^{-02}	7.3051×10^{-03}
3	3.2264×10^{-04}	4.9188×10^{-04}	4.5388×10^{-04}	2.9991×10^{-04}
4	1.4544×10^{-06}	9.9829×10^{-07}	1.5367×10^{-06}	3.6325×10^{-07}
5	6.8672×10^{-10}	3.5754×10^{-08}	9.9118×10^{-10}	7.1873×10^{-09}

Table 4. Typical Convergence Value, the Relative Euclidean Norms for Stress Path 1, OW

	$t=4$ s		$t=8$ s	
Iteration	Present work	Forward Euler	Present work	Forward Euler
1	$1.0000 \times 10^{+00}$	$1.0000 \times 10^{+00}$	$1.0000 \times 10^{+00}$	$1.0000 \times 10^{+00}$
2	3.1021×10^{-02}	3.2216×10^{-03}	1.3257×10^{-02}	2.4345×10^{-03}
3	1.0106×10^{-03}	2.1634×10^{-05}	1.9917×10^{-03}	5.6377×10^{-05}
4	5.6509×10^{-06}	7.1581×10^{-08}	8.9509×10^{-07}	1.2599×10^{-07}
5	7.9444×10^{-09}	4.7867×10^{-10}	1.0466×10^{-08}	3.1633×10^{-09}

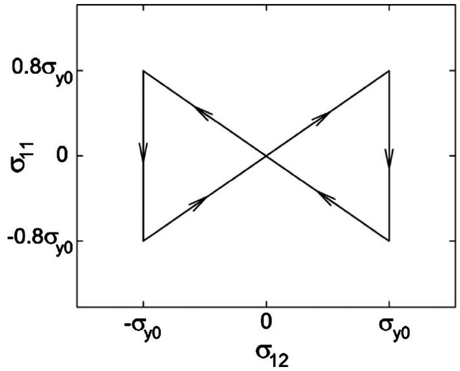

Fig. 18. Stress Path 2

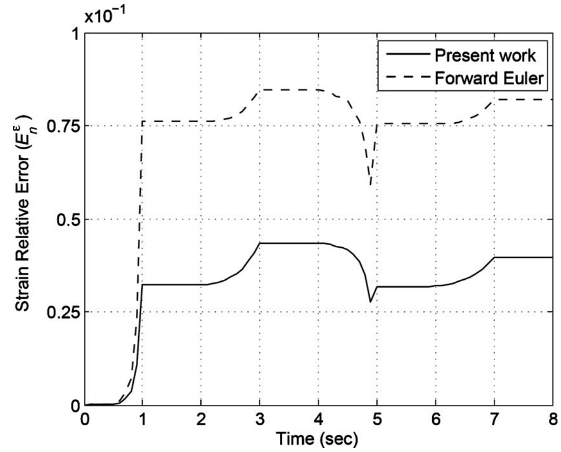

Fig. 21. Strain relative error of Path 2, OW, $\Delta t = 0.0125$ s

large considered load step. Moreover, stress versus plastic strain relation computed with the exponential-based technique for 45 load cycles is shown in Fig. 24. It should be mentioned that in stress-controlled problems, several stress updating calculations are needed to get a converged solution. As the exponential map method is more accurate in stress updating than the forward Euler method, the improvement of the accuracy in stress-controlled examples is much higher than the strain controlled problems.

To verify the ability of the new developed numerical algorithm to solve the different hardening models, the plastic axial strain at positive stress peaks of the uniaxial cycles are plotted and compared with the experiment results (Bari and Hassan 2000). Fig. 25 shows the solutions of Chaboche model, using three decomposed rules with two different values for $H_{\mathrm{nl},3}$. The prediction of the ratcheting, by the means of the Ohno-Wang kinematic hardening model, is also shown in Fig. 26. To demonstrate the effect of nonlinearity induced by the power q_i on the ratcheting simulations, three different values for this parameter, which are $q_i = 0.2/0.45/0.70$, are considered. It is worth emphasizing that the

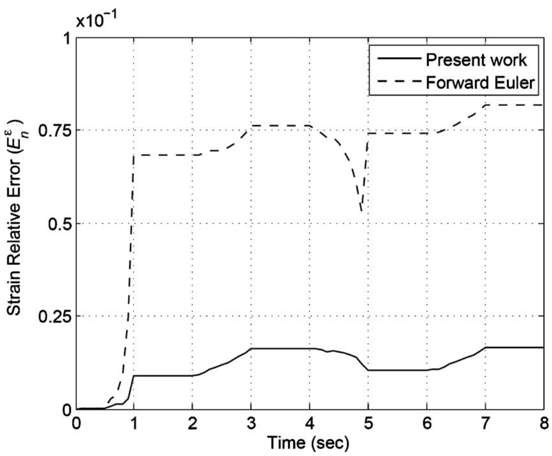

Fig. 19. Strain relative error of Path 2, Ch3, $\Delta t = 0.0125$ s

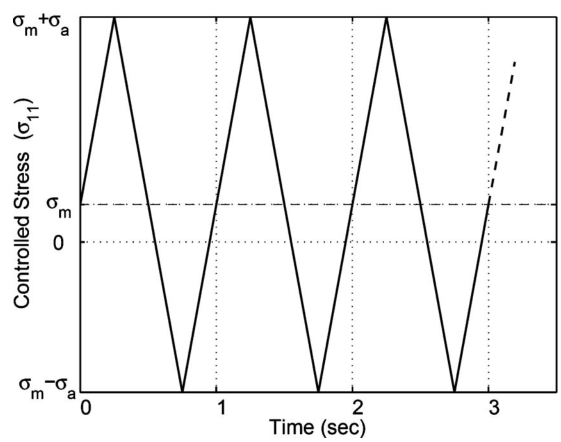

Fig. 22. Stress history for uniaxial ratcheting

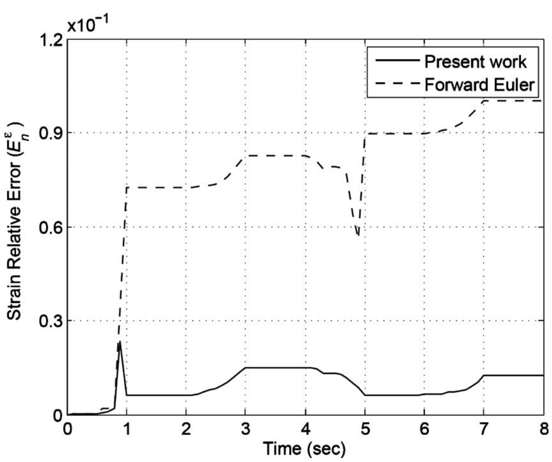

Fig. 20. Strain relative error of Path 2, Ch4T, $\Delta t = 0.0125$ s

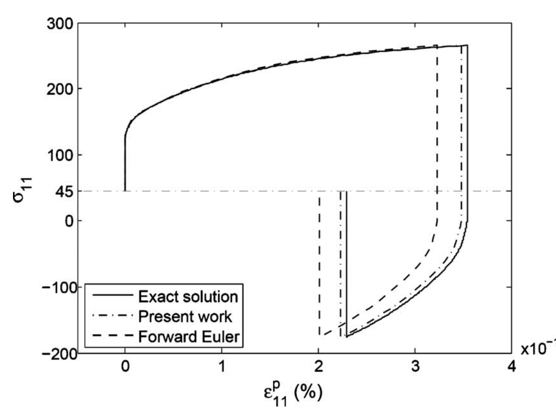

Fig. 23. Stress-plastic strain relation for the first load cycle, Ch3, $\Delta t = 0.01$ s

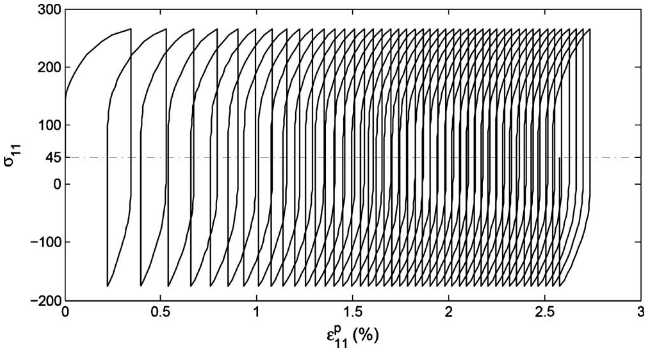

Fig. 24. Stress-plastic strain relation calculated with the new presented method for 45 load cycles, Ch3, $\Delta t = 0.001$ s

smaller the value of the q_i, the more nonlinear the decomposed rules are. In other words, if this value decreases, the rate of the ratcheting increases.

Mixed Type Control Example

A biaxial nonproportional strain history is considered. The nonzero input strain components' histories and the corresponding path are represented graphically in Figs. 27 and 28. All the stress

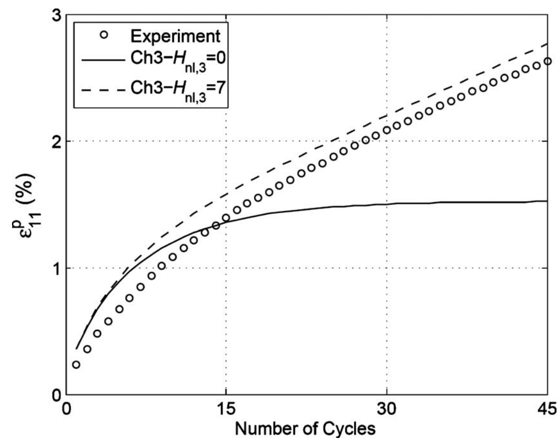

Fig. 25. Axial plastic strain at positive stress peaks of uniaxial cycles, Ch3, new presented method, $\Delta t = 0.001$ s

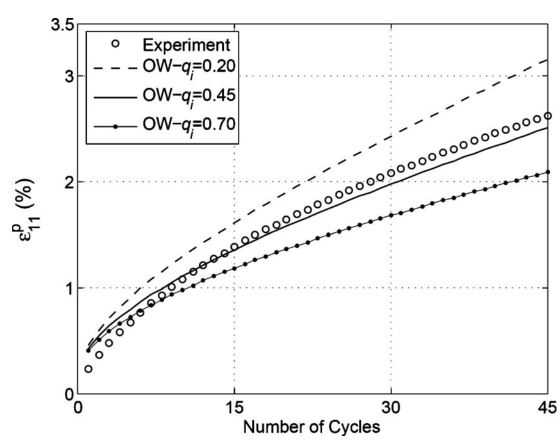

Fig. 26. Axial plastic strain at positive stress peaks of uniaxial cycles, OW, new presented method, $\Delta t = 0.001$ s

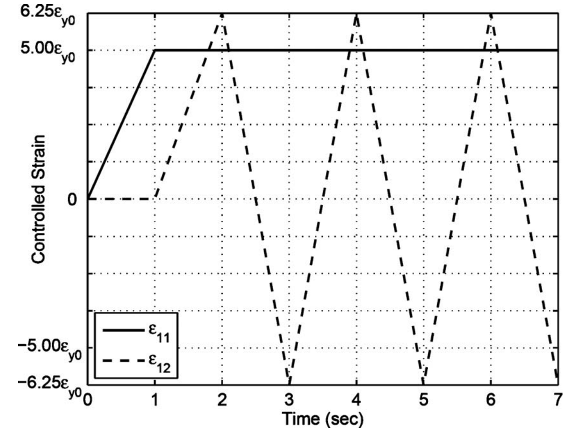

Fig. 27. Strain components history for mixed control example

components not corresponding to the two controlled-strain components are identically equal to zero. For the sake of comparison, the updated stress and strain history are calculated with the new exponential-based method and also with the forward Euler algorithm. A load step with the size of $\Delta t = 0.0125$ s is considered. The relative errors of updated stress, Eq. (85), and also updated strain, Eq. (87), are computed for Ch3, Ch4T, and OW kinematic hardening models. The results, which are illustrated in Figs. 29–34, show the performance of the exponential-based method.

Conclusions

The von-Mises yield function, in the small strain domain, along with a class of multicomponent forms of nonlinear kinematic hardening rules are considered in this study. Application of exponential-based methods in integrating constitutive equations for a class of cyclic plasticity models has been proposed. Furthermore, a detailed formulation is presented for the forward Euler method to compare the results with the new exponential-based technique. The consistent tangent operator for the exponential-based algorithm and also for the classical forward Euler algorithm is developed. This operator could be used to construct the stiffness matrix of a structure and eventually guarantees the quadratic rate of convergence for solving nonlinear simultaneous equations in a finite-element analysis. A wide range of the numerical test is carried out. As it was clearly shown, the exponential-based technique gives very accurate updated stress values that are consistent with the yield surface. Without any doubt, this robustness of the

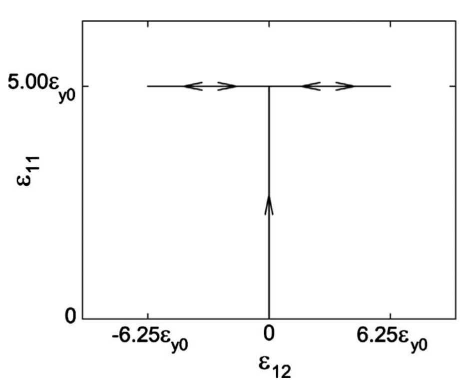

Fig. 28. Strain path for mixed control example

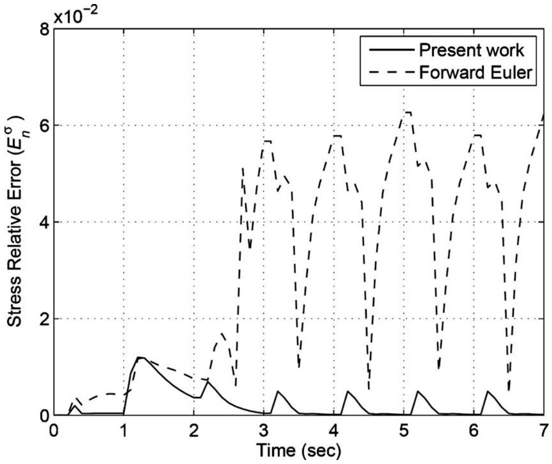

Fig. 29. Stress relative error for mixed control example, Ch3, Δt =0.0125 s

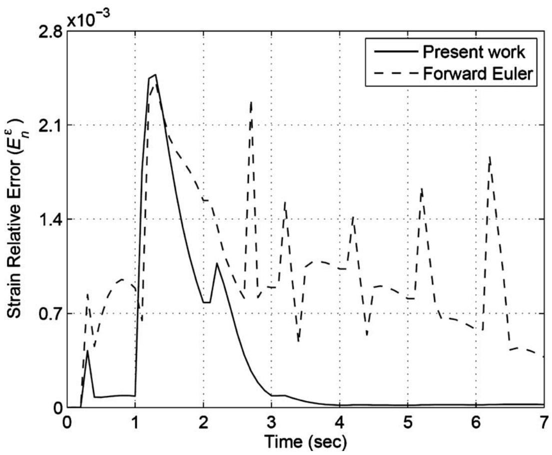

Fig. 30. Strain relative error for mixed control example, Ch3, Δt =0.0125 s

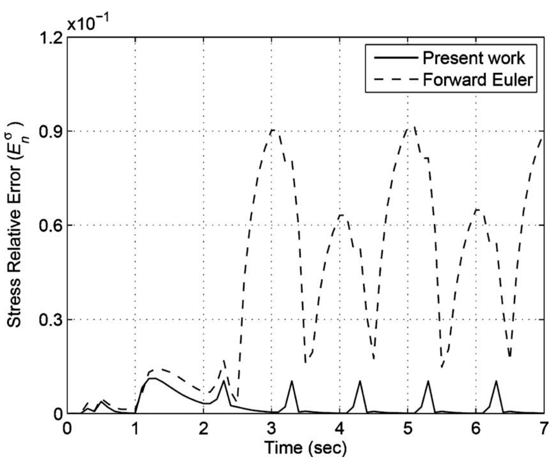

Fig. 31. Stress relative error for mixed control example, Ch4T, Δt =0.0125 s

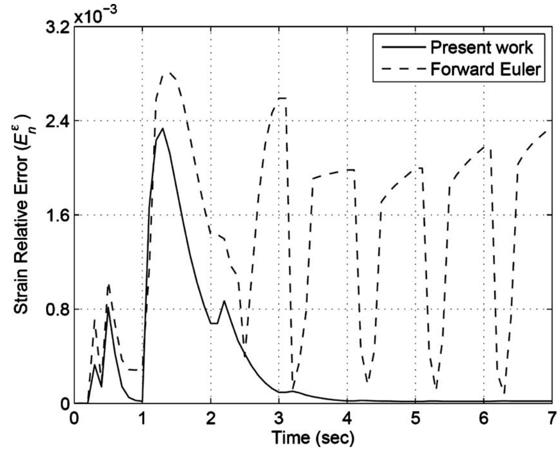

Fig. 32. Strain relative error for mixed control example, Ch4T, Δt =0.0125 s

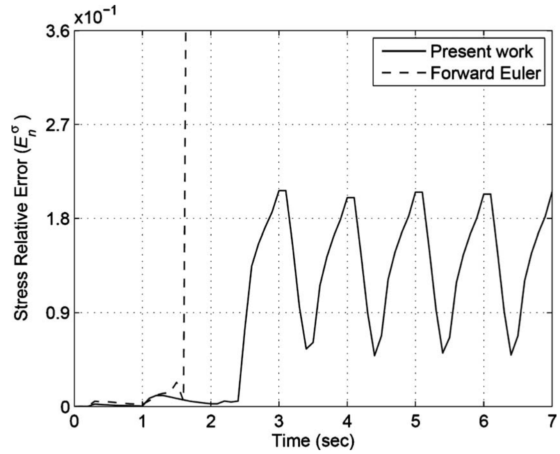

Fig. 33. Stress relative error for mixed control example, OW, Δt =0.0125 s

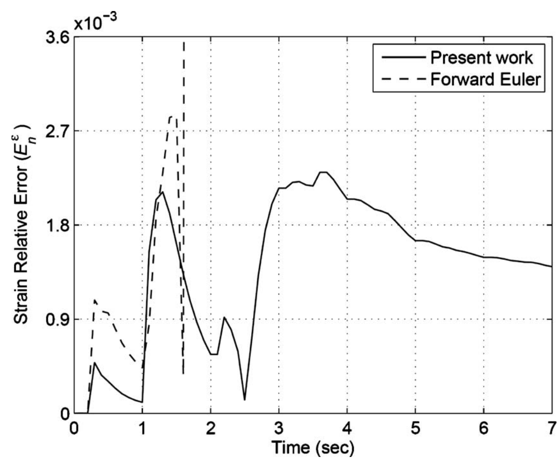

Fig. 34. Strain relative error for mixed control example, OW, Δt =0.0125 s

presented formulation would enable the analysts to enlarge the time step in the process of the stress updating and significantly reduces the computation time in the global finite-element analysis.

Appendix I. Derivatives of Parameter A_i^c for Different Kinematic Hardening Models

For Chaboche models which are presented in Eqs. (12) and (13)

$$\frac{\partial A_i^c}{\partial \mathbf{e}_{n+1}} = 0 \tag{89}$$

For Ohno-Wang model-1 which is given in Eq. (14):

$$\frac{\partial A_i^c}{\partial \mathbf{e}_{\mathbf{n+1}}} = H_{\mathrm{nl},i}\mathrm{H}\left\{(\mathbf{n}^c)^T\frac{\boldsymbol{\alpha}_{n,i}}{\|\boldsymbol{\alpha}_{n,i}\|}\right\}\mathrm{H}\left\{\boldsymbol{\alpha}_{n,i}^T\boldsymbol{\alpha}_{n,i} - \frac{3}{2}\left(\frac{H_{\mathrm{kin},i}}{H_{\mathrm{nl},i}}\right)^2\right\}\frac{\partial \mathbf{n}^c}{\partial \mathbf{e}_{n+1}}\frac{\boldsymbol{\alpha}_{n,i}}{\|\boldsymbol{\alpha}_{n,i}\|} \tag{90}$$

For Ohno-Wang model-2 which is presented in Eq. (15)

$$\frac{\partial A_i^c}{\partial \mathbf{e}_{n+1}} = H_{\mathrm{nl},i}\mathrm{H}\left\{(\mathbf{n}^c)^T\frac{\boldsymbol{\alpha}_{n,i}}{\|\boldsymbol{\alpha}_{n,i}\|}\right\}\left(\frac{H_{\mathrm{nl},i}}{H_{\mathrm{kin},i}}\|\boldsymbol{\alpha}_{n,i}\|\right)^{q_i}\frac{\partial \mathbf{n}^c}{\partial \mathbf{e}_{n+1}}\frac{\boldsymbol{\alpha}_{n,i}}{\|\boldsymbol{\alpha}_{n,i}\|} \tag{91}$$

For AbdelKarim-Ohno model which is given Eq. (16):

$$\frac{\partial A_i^c}{\partial \mathbf{e}_{n+1}} = H_{\mathrm{nl},i}H\left\{(\mathbf{n}^c)^T\frac{\boldsymbol{\alpha}_{n,i}}{\|\boldsymbol{\alpha}_{n,i}\|} - \mu_i\right\}H\left\{\boldsymbol{\alpha}_{n,i}^T\boldsymbol{\alpha}_{n,i} - \frac{3}{2}\left(\frac{H_{\mathrm{kin},i}}{H_{\mathrm{nl},i}}\right)^2\right\}\frac{\partial \mathbf{n}^c}{\partial \mathbf{e}_{n+1}}\frac{\boldsymbol{\alpha}_{n,i}}{\|\boldsymbol{\alpha}_{n,i}\|} \tag{92}$$

Appendix II. Derivatives Appeared in the Consistent Tangent Operator of the Forward Euler Method

The required formulations for forward Euler technique are as follows:

$$\frac{\partial \boldsymbol{\Sigma}'_{n+1}}{\partial \mathbf{e}_{n+1}} = \frac{\partial \mathbf{s}'_{n+1}}{\partial \mathbf{e}_{n+1}} - \frac{\partial \boldsymbol{\alpha}_{n+1}}{\partial \mathbf{e}_{n+1}} \tag{93}$$

$$\frac{\partial \mathbf{s}'_{n+1}}{\partial \mathbf{e}_{n+1}} = 2G\left(\mathbb{I} - \frac{\partial \Delta \mathbf{e}^p}{\partial \mathbf{e}_{n+1}}\right) \tag{94}$$

$$\frac{\partial \Delta \mathbf{e}^p}{\partial \mathbf{e}_{n+1}} = \frac{\partial \lambda}{\partial \mathbf{e}_{n+1}}(\mathbf{n}^c)^T + \lambda\frac{\partial \mathbf{n}^c}{\partial \mathbf{e}_{n+1}} \tag{95}$$

$$\begin{aligned}\frac{\partial \lambda}{\partial \mathbf{e}_{n+1}} = &-2wG(\mathbf{n}^c)^T\Delta\mathbf{e}\frac{d\alpha}{d\mathbf{e}_{n+1}} + 2wG(1-\alpha)\frac{\partial \mathbf{n}^c}{\partial \mathbf{e}_{n+1}}\Delta\mathbf{e} \\ &+ 2wG(1-\alpha)\mathbf{n}^c + 2w^2G(1-\alpha) \\ &\times(\mathbf{n}^c)^T\Delta\mathbf{e}\left(\frac{\partial \mathbf{n}^c}{\partial \mathbf{e}_{n+1}}\sum_{i=1}^{m}A_i^c\boldsymbol{\alpha}_{n,i}\right) + 2w^2G(1-\alpha) \\ &\times(\mathbf{n}^c)^T\Delta\mathbf{e}\left\{\left[\sum_{i=1}^{m}\boldsymbol{\alpha}_{n,i}\left(\frac{\partial A_i^c}{\partial \mathbf{e}_{n+1}}\right)^T\right]\mathbf{n}^c\right\}, \\ w = &\frac{1}{2\bar{G} - (\mathbf{n}^c)^T\sum_{i=1}^{m}A_i^c\boldsymbol{\alpha}_{n,i}}\end{aligned} \tag{96}$$

$$\frac{\partial \mathbf{n}^c}{\partial \mathbf{e}_{n+1}} = \frac{1}{\|\boldsymbol{\Sigma}^c\|}\frac{\partial \boldsymbol{\Sigma}^c}{\partial \mathbf{e}_{n+1}} - \boldsymbol{\Sigma}_{n+1}^c\left(\frac{\partial \boldsymbol{\Sigma}^c}{\partial \mathbf{e}_{n+1}}\frac{\boldsymbol{\Sigma}^c}{\|\boldsymbol{\Sigma}^c\|^3}\right)^T \tag{97}$$

$$\frac{\partial \boldsymbol{\Sigma}^c}{\partial \mathbf{e}_{n+1}} = 2G\frac{d\alpha}{d\mathbf{e}_{n+1}}\Delta\mathbf{e}^T + 2G\alpha\mathbb{I} \tag{98}$$

$$\frac{d\alpha}{d\mathbf{e}_{n+1}} = T_1\frac{dC}{d\mathbf{e}_{n+1}} + T_2\frac{dD}{d\mathbf{e}_{n+1}} \tag{99}$$

$$T_1 = \frac{1}{D}\left(\frac{C}{\sqrt{C^2 - DM}} - 1\right); \quad T_2 = -\frac{1}{D^2}\left(\frac{DM}{2\sqrt{C^2 - DM}} + \sqrt{C^2 - DM} - C\right) \tag{100}$$

$$\frac{dC}{d\mathbf{e}_{n+1}} = 2G(\mathbf{s}_n - \boldsymbol{\alpha}_n); \quad \frac{dD}{d\mathbf{e}_{n+1}} = 2(2G)^2\Delta\mathbf{e} \tag{101}$$

$$\begin{aligned}\frac{\partial a_f}{\partial \mathbf{e}_{n+1}} = &[(\mathbf{n}_{n+1}^T\boldsymbol{\Sigma}'_{n+1})^2 - \|\boldsymbol{\Sigma}'_{n+1}\|^2 + R^2]^{-1/2}\left[\left(\frac{\partial \mathbf{n}_{n+1}}{\partial \mathbf{e}_{n+1}}\boldsymbol{\Sigma}'_{n+1}\right.\right. \\ &\left.\left.+ \frac{\partial \boldsymbol{\Sigma}'_{n+1}}{\partial \mathbf{e}_{n+1}}\mathbf{n}_{n+1}\right)(\mathbf{n}_{n1}^T\boldsymbol{\Sigma}'_{n+1}) - \frac{\partial \boldsymbol{\Sigma}'_{n+1}}{\partial \mathbf{e}_{n+1}}\boldsymbol{\Sigma}'_{n+1}\right] \\ &- \frac{\partial \mathbf{n}_{n+1}}{\partial \mathbf{e}_{n+1}}\boldsymbol{\Sigma}'_{n+1} - \frac{\partial \boldsymbol{\Sigma}'_{n+1}}{\partial \mathbf{e}_{n+1}}\mathbf{n}_{n+1}\end{aligned} \tag{102}$$

Appendix III. Derivatives Appeared in Consistent Tangent Operator for the Exponential-Based Method

The following formulations are the derivatives needed for the suggested strategy:

$$\begin{aligned}\frac{\partial \mathbf{X}_{n+1}^s}{\partial \mathbf{e}_{n+1}} = &C_1\left[\Delta\hat{\boldsymbol{\Phi}}\left(\frac{\partial a}{\partial \mathbf{e}_{n+1}}\right)^T\right] + C_2\left[\Delta\hat{\boldsymbol{\Phi}}\left(\frac{\partial \Delta\hat{\boldsymbol{\Phi}}}{\partial \mathbf{e}_{n+1}}\mathbf{X}_n^s\right)^T\right] \\ &+ C_3\left(\frac{\partial \Delta\hat{\boldsymbol{\Phi}}}{\partial \mathbf{e}_{n+1}}\right) + C_4\left[\Delta\mathbf{e}\left(\frac{d\alpha}{d\mathbf{e}_{n+1}}\right)^T\right] + C_5\left[\Delta\hat{\boldsymbol{\Phi}}\left(\frac{d\alpha}{d\mathbf{e}_{n+1}}\right)^T\right] \\ &+ C_6\left[\Delta\hat{\boldsymbol{\Phi}}\left(\frac{\partial \Delta\hat{\boldsymbol{\Phi}}}{\partial \mathbf{e}_{n+1}}\Delta\mathbf{e}\right)^T + \Delta\hat{\boldsymbol{\Phi}}\Delta\hat{\boldsymbol{\Phi}}^T\right] + C_7\left[\Delta\hat{\boldsymbol{\Phi}}\left(\frac{\partial b}{\partial \mathbf{e}_{n+1}}\right)^T\right] \\ &+ C_8\mathbb{I}\end{aligned} \tag{103}$$

$$C_1 = \Delta\hat{\boldsymbol{\Phi}}^T\mathbf{X}_n^s + \alpha\frac{2G}{R}X_n^0(\Delta\hat{\boldsymbol{\Phi}}^T\Delta\mathbf{e}); \quad C_2 = a - 1$$

$$C_3 = (a-1)(\Delta\hat{\boldsymbol{\Phi}}^T\mathbf{X}_n^s) + (a-1)\alpha\frac{2G}{R}X_n^0(\Delta\hat{\boldsymbol{\Phi}}^T\Delta\mathbf{e}) + bX_n^0$$

$$C_4 = \frac{2G}{R}X_n^0; \quad C_5 = (a-1)\alpha\frac{2G}{R}X_n^0(\Delta\hat{\boldsymbol{\Phi}}^T\Delta\mathbf{e})$$

$$C_6 = (a-1)\alpha\frac{2G}{R}X_n^0; \quad C_7 = X_n^0; \quad C_8 = \alpha\frac{2G}{R}X_n^0 \tag{104}$$

$$\frac{\partial X_{n+1}^0}{\partial \mathbf{e}_{n+1}} = D_1 \frac{\partial b}{\partial \mathbf{e}_{n+1}} + D_2 \left(\frac{\partial \Delta \hat{\mathbf{\Phi}}}{\partial \mathbf{e}_{n+1}} \mathbf{X}_n^s \right) + D_3 \frac{d\alpha}{d\mathbf{e}_{n+1}} + D_4 \left(\frac{\partial \Delta \hat{\mathbf{\Phi}}}{\partial \mathbf{e}_{n+1}} \Delta \mathbf{e} + \Delta \hat{\mathbf{\Phi}} \right) + D_5 \frac{\partial a}{\partial \mathbf{e}_{n+1}} \tag{105}$$

$$D_1 = \Delta \hat{\mathbf{\Phi}}^T \mathbf{X}_n^s + \alpha \frac{2G}{R} X_n^0 (\Delta \hat{\mathbf{\Phi}}^T \Delta \mathbf{e}); \quad D_2 = b; \quad D_3 = b \frac{2G}{R} X_n^0 (\Delta \hat{\mathbf{\Phi}}^T \Delta \mathbf{e})$$

$$D_4 = b\alpha \frac{2G}{R} X_n^0; \quad D_5 = X_n^0 \tag{106}$$

$$\frac{d\alpha}{d\mathbf{e}_{n+1}} = T_1 \frac{dC}{d\mathbf{e}_{n+1}} + T_2 \frac{dD}{d\mathbf{e}_{n+1}} \tag{107}$$

$$T_1 = \frac{1}{D} \left(\frac{C}{\sqrt{C^2 - DM}} - 1 \right); \quad T_2 = -\frac{1}{D^2} \left(\frac{DM}{2\sqrt{C^2 - DM}} + \sqrt{C^2 - DM} - C \right) \tag{108}$$

$$\frac{dC}{d\mathbf{e}_{n+1}} = \frac{2G}{R} X_n^0 \mathbf{X}_n^s; \quad \frac{dD}{d\mathbf{e}_{n+1}} = 2 \left(\frac{2G}{R} X_n^0 \right)^2 \Delta \mathbf{e} \tag{109}$$

$$\frac{\partial \Delta \hat{\mathbf{\Phi}}}{\partial \mathbf{e}_{n+1}} = \frac{1}{\|\Delta \mathbf{\Phi}\|} \frac{\partial \Delta \mathbf{\Phi}}{\partial \mathbf{e}_{n+1}} - \frac{1}{\|\Delta \mathbf{\Phi}\|} \left[\Delta \hat{\mathbf{\Phi}} \left(\frac{\partial \Delta \mathbf{\Phi}}{\partial \mathbf{e}_{n+1}} \Delta \hat{\mathbf{\Phi}} \right)^T \right] \tag{110}$$

$$\begin{aligned} \frac{\partial \Delta \mathbf{\Phi}}{\partial \mathbf{e}_{n+1}} &= \mathbb{I} + w \left(\sum_{i=1}^m A_i^c \boldsymbol{\alpha}_{n,i} \right) (\mathbf{n}^c)^T + w \left[\left(\sum_{i=1}^m A_i^c \boldsymbol{\alpha}_{n,i} \right) \Delta \mathbf{e}^T \right] \frac{\partial \mathbf{n}^c}{\partial \mathbf{e}_{n+1}} \\ &+ w (\mathbf{n}^c)^T \Delta \mathbf{e} \sum_{i=1}^m \boldsymbol{\alpha}_{n,i} \left(\frac{\partial A_i^c}{\partial \mathbf{e}_{n+1}} \right)^T + w^2 (\mathbf{n}^c)^T \Delta \mathbf{e} \left(\sum_{i=1}^m A_i^c \boldsymbol{\alpha}_{n,i} \right) \\ &\times \left(\frac{\partial \mathbf{n}^c}{\partial \mathbf{e}_{n+1}} \sum_{i=1}^m A_i^c \boldsymbol{\alpha}_{n,i} \right)^T + w^2 (\mathbf{n}^c)^T \Delta \mathbf{e} \left(\sum_{i=1}^m A_i^c \boldsymbol{\alpha}_{n,i} \right) \\ &\times \left\{ \left[\sum_{i=1}^m \boldsymbol{\alpha}_{n,i} \left(\frac{\partial A_i^c}{\partial \mathbf{e}_{n+1}} \right)^T \right] \mathbf{n}^c \right\}^T, \\ w &= \frac{1}{2\bar{G} - (\mathbf{n}^c)^T \sum_{i=1}^m A_i^c \boldsymbol{\alpha}_{n,i}} \end{aligned} \tag{111}$$

$$\frac{\partial \mathbf{n}^c}{\partial \mathbf{e}_{n+1}} = \alpha \frac{2G}{R} \mathbb{I} + \frac{2G}{R} \left[\Delta \mathbf{e} \left(\frac{d\alpha}{d\mathbf{e}_{n+1}} \right)^T \right] \tag{112}$$

$$\frac{\partial a}{\partial \mathbf{e}_{n+1}} = b \frac{2G}{R} \left[(1-\alpha) \frac{\partial \Delta \mathbf{\Phi}}{\partial \mathbf{e}_{n+1}} \Delta \hat{\mathbf{\Phi}} - \|\Delta \mathbf{\Phi}\| \frac{d\alpha}{d\mathbf{e}_{n+1}} \right] \tag{113}$$

$$\frac{\partial b}{\partial \mathbf{e}_{n+1}} = a \frac{2G}{R} \left[(1-\alpha) \frac{\partial \Delta \mathbf{\Phi}}{\partial \mathbf{e}_{n+1}} \Delta \hat{\mathbf{\Phi}} - \|\Delta \mathbf{\Phi}\| \frac{d\alpha}{d\mathbf{e}_{n+1}} \right] \tag{114}$$

References

Abdel-Karim, M., and Ohno, N. (2000). "Kinematic hardening model suitable for ratcheting with steady-state." *Int. J. Plast.*, 16, 225–240.

Abdel-Karim, M. (2009). "Modified kinematic hardening rules for simulations of ratchetting." *Int. J. Plast.*, 25, 1560–1587.

Armstrong, P. J., and Frederick, C. O. (1966). "A mathematical representation of the multiaxial Bauscinger effect." *CEGB Rep. No. RD/B/N731*, Central Electricity Generating Board, Berkeley, U.K.

Artioli, E., Auricchio, F., and Beirão da Veiga, L. (2006). "A novel 'optimal' exponential-based integration algorithm for von-Mises plasticity with linear hardening: Theoretical analysis on yield consistency, accuracy, convergence and numerical investigations." *Int. J. Numer. Methods Eng.*, 67(4), 449–498.

Artioli, E., Auricchio, F., and Beirão da Veiga, L. (2007). "Second-order accurate integration algorithms for von-Mises plasticity with a nonlinear kinematic hardening mechanism." *Comput. Methods Appl. Mech. Eng.*, 196, 1827–1846.

Auricchio, F., and Beirão da Veiga, L. (2003). "On a new integration scheme for von-Mises plasticity with linear hardening." *Int. J. Numer. Methods Eng.*, 56, 1375–1396.

Bari, S., and Hassan, T. (2000). "Anatomy of coupled constitutive models for ratcheting simulation." *Int. J. Plast.*, 16, 381–409.

Besseling, J. F. (1958). "A theory of elastic, plastic, and creep deformations of an initially isotropic material." *ASME J. Appl. Mech.*, 25, 529–536.

Chaboche, J. L., Dang-Van, K., and Cordier, G. (1979). "Modelization of strain memory effect on the cyclic hardening of 316 stainless steel." *Proc., Transactions of the 5th Int. Conf. on Structural Mechanics in Reactor Technology*, No. Div L in 11/3, Berlin.

Chaboche, J. L. (1986). "Time-independent constitutive theories for cyclic plasticity." *Int. J. Plast.*, 2, 149–188.

Chaboche, J. L. (1991). "On some modifications of kinematic hardening to improve the description of ratcheting effects." *Int. J. Plast.*, 7, 661–678.

Hassan, T., and Kyriakides, S. (1994a). "Ratcheting of cyclically hardening and softening materials. Part I: Uniaxial behavior." *Int. J. Plast.*, 10, 149–184.

Hassan, T., and Kyriakides, S. (1994b). "Ratcheting of cyclically hardening and softening materials. Part II: Multiaxial behavior." *Int. J. Plast.*, 10, 185–212.

Hong, H.-K., and Liu, C.-S. (1999). "Internal symmetry in bilinear elastoplasticity." *Int. J. Non-linear Mech.*, 34, 279–288.

Hong, H.-K., and Liu, C.-S. (2000). "Internal symmetry in the constitutive model of perfect elastoplasticity." *Int. J. Non-linear Mech.*, 35, 447–466.

Hong, H.-K., and Liu, C.-S. (2001). "Lorentz group on Minkowski spacetime for construction of the two basic principles of plasticity." *Int. J. Non-linear Mech.*, 36, 679–686.

Hopperstad, O. S., and Remseth, S. (1995). "A return mapping algorithm for a class of cyclic plasticity models." *Int. J. Numer. Methods Eng.*, 38, 549–564.

Kang, G. (2004). "A visco-plastic constitutive model for ratcheting of cyclically stable materials and its finite element implementation." *Mech. Mater.*, 36, 299–312.

Kobayashi, M., and Ohno, N. (2002). "Implementation of cyclic plasticity models based on a general form of kinematic hardening." *Int. J. Numer. Methods Eng.*, 53, 2217–2238.

Liu, C.-S. (2003). "Symmetry groups and the pseudo-Riemann spacetimes for mixed-hardening elastoplasticity." *Int. J. Solids Struct.*, 40, 251–269.

Liu, C.-S. (2004). "Internal symmetry groups for the Drucker-Prager material model of plasticity and numerical integrating methods." *Int. J. Solids Struct.*, 41, 3771–3791.

Mroz, Z. (1967). "On the description of anisotropic work hardening." *J. Mech. Phys. Solids*, 15, 163–175.

Ohno, N., and Wang, J. D. (1993). "Kinematic hardening rules with critical state of dynamic recovery. Part I: Formulations and basic features for ratcheting behavior." *Int. J. Plast.*, 9, 375–390.

Prager, W. (1956). "A new method of analyzing stresses and strains in work hardening plastic solids." *J. Appl. Mech.*, 23, 493–496.

Rezaiee-Pajand, M., and Nasirai, C. (2007). "Accurate integration scheme for von-Mises plasticity with mixed-hardening based on exponential maps." *Eng. Comput.*, 24(6), 608–635.

Rezaiee-Pajand, M., and Sinaie, S. (2009). "On the calibration of the Chaboche hardening model and a modified hardening rule for uniaxial ratcheting prediction." *Int. J. Solids Struct.*, 46, 3009–3017.